Spatiotemporal transcriptomic analyses reveal molecular gradient patterning during development and the tonotopic organization along cochlear axis

Mengzhen Yan[1,2,#], Penghui Zhang[1,2,#], Yafan Wang[1,2,#], Haojie Wang[2,3,#], Junhong Li[4], Xiang Guo[5], Xiangyao Zeng[6], Yushan Gao[1,2], Jieran Dong[7], Bicheng Zhu[1], Di Deng[4], Lu Ma[6], Yong Feng[6,7,8,9], Hua-Jun Wu[3,10,11,*], Yu Zhao[4,*] and Jun Li[1,*]

[1]Chengdu Institute of Biology, Chinese Academy of Sciences, Chengdu 610213, China

[2]University of Chinese Academy of Sciences, Beijing, China.

[3]Key Laboratory of Carcinogenesis and Translational Research (Ministry of Education/Beijing), Peking University Cancer Hospital and Institute, Beijing100142, China.

[4]Department of Otolaryngology-Head & Neck Surgery, West China Hospital, Sichuan University, Chengdu 610041, China

[5]Institute of Blood Diseases, Department of Hematology, Sichuan Academy of Medical Sciences & Sichuan Provincial People's Hospital, School of Medicine of University of Electronic Science and Technology of China, Sichuan, Chengdu 610000, China.

[6]Institute of Cytology and Genetics, Hengyang Medical School, University of South China, Hengyang 421000, China

[7]College of Agronomy, Sichuan Agricultural University, Chengdu 611130, China.

[8]Department of Otorhinolaryngology, The Affiliated Changsha Central Hospital, Hengyang Medical School, University of South China, Changsha 410028, China

[9]Institute of Otorhinolaryngology, Head and Neck Surgery, University of South China, Changsha 410028, China

[10]MOE Key Lab of Rare Pediatric Diseases & Institute for Future Sciences, University of South China, Changsha 410008, China

[11]Department of Biomedical Informatics, School of Basic Medical Sciences, Peking University Health Science Center, Beijing 100191, China.

[12]Center for Precision Medicine Multi-Omics Research, Institute of Advanced Clinical Medicine, Peking University, Beijing 100191, China.

[#]Authors contributed equally to this work.

*Authors for correspondence:

Jun Li, Ph.D. Tel: +86 028 82890981

Email: lijun@cib.ac.cn

Yu Zhao, M.D. Tel: +86 028 85422436

Email: yuzhao@wchscu.edu.cn

Huajun Wu, Ph.D. Tel: +86 010 82805976

Email: hjwu@pku.edu.cn

Abstract:

The cochlea is a highly specialized organ, responsible for auditory functions, yet its development, spatial molecular profiles, and structural basis for hearing function remain poorly understood due to its structural complexity and intricate organization of various cell types. Disruption of cochlear architecture and development process can lead to cochlear malfunction, resulting in hearing defects, including frequency discrimination impairments and hearing loss. In this study, we present the first comprehensive spatiotemporal single-cell atlas of the cochlea, unveiling dynamic gene expression patterns and cellular patterning during development and adulthood. By integrating the spatial transcriptomics, normal single-cell transcriptomics, and RNA *in situ* detection, our analyses revealed distinct temporal gene expression profiles across the apical, middle, and basal regions of cochlea. Notably, spatial differential gene expression analyses uncovered regional heterogeneity among hair cell and spiral ganglion neuron subtypes, including differences in cell composition, cell-cell interactions, spatial localization. These findings suggest a cellular and molecular basis for sound frequency discrimination and sensitivity gradients along cochlear axis. Our spatiotemporal analyzes of the mouse cochlea provides a valuable resource for inner ear developmental research and offers insights into the structural, cellular, and molecular mechanisms underlying the tonotopic organization in mammals, and how their disrupting can lead to hearing impairment.

Keywords: spatiotemporal transcriptomics, hair cell, spiral ganglion neuron, deafness genes, cochlear development, tonotopic organization

Introduction

The inner ear is one of the most structurally and functionally complex organs in vertebrates, comprising the cochlea and vestibular apparatus [1]. The cochlea is responsible for converting sound waves into neural signals, while the vestibular system aids in maintaining equilibrium [2, 3]. Inner ear development is a highly coordinated process of gene expression regulation, cellular differentiation, morphogenesis, and signaling pathway activation [3, 4]. The intricate architecture of inner ear is crucial for its sensory functions, and most genetic variations affecting the structure of inner ear will cause sensory impairments. Cochlear and vestibular dysfunctions can cause significant auditory and balance disorders, such as congenital hearing loss, age-related hearing degeneration, and vestibular disorders, highlighting the need for deeper insights into inner ear development and function [3, 5]. Sensorineural hearing loss (SNHL) is one of the most prevalent chronic diseases, often caused by aging and noise overexposure. SNHL typically affects high-frequency regions above 4 kHz, though low and mid-frequency regions may also be involved depending on the etiology [6-8]. The cochlea's sensitivity to sound frequencies exhibits a tonotopic gradient along its longitudinal axis, from the base to the apex [9]. Studies showed that specific cell types or certain spatial regions are more prone to damage under stresses, ototoxic drug exposure, or during aging [10-12]. For instance, hair cell loss or spiral ganglion neuron (SGN) damages are more predominant in the basal region during aging [10]. Despite significant research, the molecular and cellular mechanisms underlying tonotopic organization and frequency-specific damage remain incompletely understood,

in part due to the complexity and inaccessibility of this deeply embedded organ [10, 13-15]. Deciphering these mechanisms is essential for understanding the cochlear developmental patterning of cochlea and etiology of hearing loss across different frequency ranges, providing potential guidance to the development of targeted therapeutic strategies.

Recent advances in single-cell transcriptomics have revolutionized our understanding of inner ear biology, including developmental [13, 16-18], aged-related hearing loss (ARHL) [19], noised induced hearing loss [20], ototoxic hair cell death [21], and hair cell regeneration [22]. This technology provides high-resolution insights into cell population heterogeneity within the inner ear, allowing for the identification of novel cell types and developmental trajectories that traditional bulk RNA sequencing approaches often miss. For example, single-cell transcriptomics has facilitated the identification of rare cells or transition cell types involved in hair cell regeneration [22, 23], and new subtypes of SGNs in the cochlea [24-26]. These insights are invaluable for understanding cellular contributions to inner ear structure and function, and for identifying potential therapeutic targets.

However, while single-cell transcriptomics has certain limitations [27], notably the loss of spatial context, which is essential for understanding inner ear function. The spatial organization of cells is often disrupted during tissue dissociation, obscuring key insights into cell localization and interactions within the broader tissue structure [28]. For instance, while single-cell transcriptomic studies have uncovered different SGNs subtypes [24, 26]. Their spatial distribution along the tonotopic axis remains unclear.

Recent immunostaining studies have shown that type I SGN exhibit differential distribution across cochlear regions [10], but the molecular mechanisms governing this remain elusive, partly due to the loss of spatial information in scRNA-seq data.

Spatial transcriptomics has emerged as a transformative approach, maintaining the spatial organization of cells while providing transcriptomic data [27]. Spatial transcriptomics map gene expression directly onto tissue sections, revealing spatial patterns that contribute to developmental gradients and regional specialization in the inner ear. Recent advances have enabled researcher to explore the spatial and temporal dynamics of gene expression in complex tissues like the heart [29, 30] and brain [31]. In the context of the inner ear, spatial transcriptomics allows for precise localization of gene expression, facilitating the study of tonotopic organization, development, and pathology. It also enables the integration of transcriptomic data with morphological scRNA-seq findings, helping validate cellular identities in relation to specific tissue structures [28, 30]. Additionally, spatial transcriptomics offers insights into microenvironments and cell-cell interactions that drive organ development and function [32].

In this study, we applied spatial transcriptomics at different stages of cochlear development. The approach identified typical cell subtypes and their spatial organization, revealing dynamic patterns of gene expression, cell subtype localization, and intercellular communication. We found that SGN and hair cell subtypes exhibit finely tuned spatial arrangements. Furthermore, cell communication analyses uncovered both canonical and novel cell chats between hair cells, SGNs, and other

cochlear cell types. These findings provide new insights into the molecular mechanisms underlying the tonotopic organization of auditory sensitivity along the cochlear axis. By integrating spatial and single-cell transcriptomics, this study advances our understanding of the structural and functional complexity of the inner ear, offering insights into therapeutic strategies aimed at hearing loss.

Results

Spatiotemporal characterization of cochlear cell types at different stages

The intricate structure of the cochlea serves as the basis for its complex auditory functions. To elucidate the molecular mechanisms of cochlear morphogenesis and its functional establishment during development, we conducted spatial transcriptomic analyses of the inner ear across three different important stages, embryonic stage 17.5 (E17.5), postnatal stage 8 (P8), and adult stage (2M), respectively (Fig. 1a). During development, the structures of the inner ear undergo dynamic changes, ultimately forming a complex, highly specialized architecture in adult stage (Fig. 1b). The cochlea is a spiral structure rich in chambers, formed by various cell types that are intricately and spatially organized in an ordered manner (Fig. 1b) [1]. The spatiotemporal single-cell atlases were first established from these spatial transcriptomic data. After removing blank regions, a total of 5,545, 10,214 and 7,414 spots were obtained from single E17.5, P8 and 2M mouse cochlea section samples at a resolution of 10 μm, respectively.

In general, the spatial transcriptomic data have lower resolution and relatively low quality of cell clustering, comparing to routine single-cell level transcriptomic data [27]. Integration of scRNA-seq and spatial RNA-seq will facilitate the spatial data analyses,

which will enhance their powers for each other. Therefore, the E17.5, P8 cochlear scRNA-seq data from previous publications [17], and the adult cochlear single-nucleus RNA-seq (snRNA-seq) data from our previous publication [33] were re-analyzed and compared with our spatial RNA-seq data. The gene markers from previous scRNA-seq studies [17, 24, 26, 33] were used for spatial single cell clustering and cell type identification. Based on the gene expression profile, the histological location and previous reported markers, 22 cell types were annotated in E17.5 cochlea (Fig. S1a), 28 cell types in P8 cochlea (Fig. 1b), and 21 cell types in 2M cochlea (Fig. S1c), respectively.

According to the spatial distribution, all cell types from each dataset were first briefly split into 8 groups including surrounding structure, fibrocyte, neuron, Schwann cell, Reissner's membrane, stria, root cell/spindle cell, and organ of Corti (OC) (Fig. 1d) (Table S1). Neither root cell nor spindle cell was identified in the dataset of E17.5 cochlea. But they are clearly identified in P8 and adult cochlea single-cell atlases with markers (*Aqp5* and *Slc26a4*), suggesting these cells were differentiated between E17.5 and P8 stages (Fig. 1c, d, and S1). The surrounding structure mainly contained outer structure (identified by *Col1a1* and *Mmp9*), Neutrophils (identified by *Retnlg* and *Lcn2*), chondrocyte and pericytes (identified by *Mgp*, *Slc38a2* and *Gja4*), and Osteoblast (identified by *Panx3* and *Satb2*) (Fig. 1c). Fibrocytes of cochlea mainly distributed in the spiral ligament and limbus [34]. With the spatial location and specific markers, spiral ligament (SLg) fibrocyte and spiral limbus (SLb) fibrocyte were discovered in every dataset. And 4 subtypes of SLg fibrocyte were identified by *Car3* and *Otor* at P8

dataset. The neurosensory epithelium of cochlea plays a crucial role in auditory sensory, which mainly comprises OC and SGN. With the known neuron markers (*Nefh*, *Snap25*, *Nefl* and *Meg3*) [35-37], the neuron cells were found mainly existed in the three regions near the cochlea duct (Fig. 1c, S1b and c). Multiple cells identified in the OC revealed the high cellular heterogeneity during hearing establishment and maturation, 7 cell types for E17.5 sample, 10 cell types for P8 sample and 6 cell types for adult sample. As for P8 OC, interdental cell (identified by *Otoa* and *Rspo2*), inner sulcus cell (identified by *Aqp4*), inner phalangeal cell/inner border cell (identified by *Far1* and *Tecta*), Hensen's cell and outer sulcus cell (identified by *Frzb* and *Umodl1*), outer hair cell (OHC) and inner hair cell (IHC) (identified by *Otof*) and Deiter cell/pillar cell (identified by *Lgr6*) were observed (Fig. 1d).

Spatial organization of cochlear lateral wall cell types

Several typical cochlear structures or cell types were further spatially analyzed in details to validate spatial single cell atlas. The lateral wall, balancing the endocochlear potential, was composed of stria vascularis and spiral ligament, which is one of important parts of the scala media [34]. There were three cell types in the location of stria vascularis from E17.5 and P8 samples, including basal cells, intermediate cells and marginal cells (identified by *Dnase1*, *Hpse* and *Dct*, respectively) (Fig. 2 and S2). The identical features of bubble and UMAP plotting revealed comparable quality of the spatial data to the routine single-cell level RNA-seq data (Fig. 2c, S2b and c), according to the marker genes for each lateral wall cell types [17, 33]. But only basal cells and marginal cells were annotated in the adult dataset, using *Dct* and *Kcne1* markers (Fig.

S1c, d). The intermediate cells were not identified, revealing less quality of the adult cochlear data, probably due to ossified structures in adult cochlea which hinders the tissue sections. In order to confirm the cell type annotation, RNA *in situ* assays targeting these markers above were performed. As shown in our results, *Dnase1* and *Enpep* are expressed in the stria vascularis specifically, which have not been reported. Next root cell/spindle cell were identified between outer sulcus cell and stria vascularis, with specific high expression of *Aqp5* and *Kcne4* (Fig. 2b, c), consistent with our previous study [33].In addition, four types of fibrocytes were identified in the lateral wall, based on known markers (Fig. S1d, S2) [20].

Temporal expression pattern changes of cochlear neuron cells

In the cochlea, spiral ganglion neurons (SGNs) are the primary neurons responsible for conveying sound signals detected by the hair cells of the OC (Fig. 3a). The spatial data analyses clearly identified SGNs in the exact regions where SGNs are supported to locate (Fig. 3a). The SGN neurons are reported to have two main subtypes: Type I and Type II, constituting of 90-95% and 5%-10% of the total, respectively. Type I SGNs were further divided into subtype Ia, Ib, and Ic [35, 37]. Our recent study confirmed these subtypes and identified an additional subtype, type III (Fig. 3b). Due to close similarity of molecular features and mosaic distribution of each SGN subtype, it is challenging to further identify each SGN subtype from these spatial data. Since our previous single-cell atlas data yielded higher resolution than the spatial data, previous scRNA-seq data were retrieved and reanalyzed to facilitate the spatial data analyses in this study (Fig. 3b). To validate the spatial data, RNA *in situ* detections of several SGN

markers were performed on the cochlear section. *Meg3* was highly expressed mainly in neuronal type I (Fig. 3b). The results showed that *Meg3* was expressed in neurons at all three sites of cochlear (apical, middle, and basal) (Fig. S3-1a), consistent with its painting profile in cochlear spatial section. In addition, the RNA *in situ* result of *Cend1* also showed the same spatial pattern to the chip data (Fig. S3-1b).

The supporting cells of SGNs, Schwann cells were also identified in similar regions around SGNs (Fig. S3-2a). The spatial data revealed that Schwann cells into three subtypes (Fig. S3-2b), Type I, Type II, and Type III, each displaying unique gene expression profiles (Fig. S3-2c, e). Type I Schwann cells are characterized by elevated expression levels of *Prx*, *Plp1*, and *Pllp*, suggesting their role in myelination processes (Fig. S3-2c) [38]. The RNA *in situ* results validate the expression of *Prx* (Fig. S3-2c, f). Type II Schwann cells show high expression of *Clu* and *Fabp7*, indicating a potential involvement in lipid metabolism and cellular stress responses (Fig. S3-2c) [39]. Meanwhile, Type III Schwann cells have distinct expression patterns with genes like *Smpd3*, *Htra1*, and *Ly6e* (Fig. S3-2c). These expression profiles underscore the functional diversity within Schwann cell populations and their specialized roles in supporting neural function in the inner ear. The accuracy of our spatial transcriptome data was validated by our previous single-cell transcriptome data, where these genes were equally specifically expressed in Schwann cells (Fig. S3-2d). The expression analyses of SGNs and their supporting Schwann cells together demonstrated a good consistency of spatial data with routine single-cell transcriptomic data and RNA *in situ* detection data, revealing the quality of our spatial single-cell atlas.

Further, the spatiotemporal dynamics of SGN development were analyzed using these spatial data from different stages. To explore the molecular changes that occur within the neuronal differentiation continuum and maturation, we fitted a principal tree in diffusion space. The tip of the branch that was enriched with E17.5 neurons was selected as a root and pseudotime was subsequently calculated as the distance on the tree from that root. The tree was then represented into a dendrogram recapitulating a branched trajectory based on the transcriptional similarity of pseudotime-ordered cells (Fig. 3c and S3-1c). The resulting tree accurately reflected developmental stages and the branching features. To investigate the dynamic transcriptional changes along the individual segments of the trajectories and discover transcription and signaling genes with likely functions in SGN differentiation, we used differential gene expression approaches that characterize pseudotime-ordered molecular trajectories. Focusing on genes with significant variations (Fig. 3c and S3-1d), we observed that the shared, unspecialized neurons' trajectory was characterized by rapid downregulation of genes commonly associated with early neuronal differentiation processes (*Rpl4* or *Tubb2b*), and upregulation of genes that are involved in specification events in cochlea and other systems (*Snap25*, *Spp1*, etc.). The bubble diagram more visually illustrates the dynamics of these genes during development (Fig. S3-1d). The differential marker gene expression analyses revealed the relative higher expression of *Snap25*, *Spp1* and *Atp1b1* in adult neurons, while *Rps7*, *Rpl5*, *Eef1a1*, *Tpt1*, *Tuba1a*, *Rpl4* and *Tubb2b* showed expression at earlier stages (Fig. 3c and S3-1d).

This spatiotemporal dynamic gene expression pattern of SGN was further validated

by immunostaining with Calb2, which was specifically expressed in Type III and Type Ia SGN subtypes (Fig. 3b and d) [10]. At E17.5 stage, the highest expression level of Calb2 was detected at apical region, medium at middle, and weak at the basal region (Fig. 3d, left). At P8, relatively averaged expression levels were observed in these regions (Fig. 3d, middle). Comparing to E17.5 stage, the adulthood displayed a reversed expression pattern that the basal region has the highest expression level of Calb2 signals (Fig. 3d, right). These spatiotemporal dynamics of gene expressions reflected the molecular mechanism of development and maturation of SGNs across the progression from E17.5 to adulthood.

Gradient expression of neuronal marker genes and spatial organization of cochlear neuron cells

By leveraging the advantages of spatial transcriptomics, we conducted local and spatial single cell analyses, from apical to basal regions of cochlea. Neuron cells from three distinct regions (apical, middle, and basal) were isolated according to the spatial coordinates from the total spatial single cell atlas (Fig. 4a and S4a, d). After pairwise comparisons between apical-basal, apical-middle, and middle-basal neurons, differentially expression genes (DEGs) were initially obtained. Then by intersecting the neuron-specific gene list from snRNA dataset and spatial dataset itself (Table S1), 323, 470 and 1587 genes for E17.5, P8 and adult datasets were finally left, respectively (Table S2).

For E17.5 spatial dataset, the SGNs from apical, middle, and basal regions were extracted from the total spatial single cell atlas (Fig. S4a). The differential expression

study clearly revealed that *Nefm*, *Nefl*, *Trim2*, and *Sema3e* genes were highly expressed at the apical region and relatively low in the basal region (Fig. S4b, c). Vice versa, *Nsg1* and *Cd200* genes showed highest expression at the basal region (Fig. S4b, c). Two obvious contrary expression patterns were also observed at P8 stage. Genes like *Nefh*, *Cend1*, and *Calb2* were expressed strongest at basal region, but *Sema3e*, *Rian Myo16*, and *Cdh9* were expressed strongest at the apical region (Fig. 4b, c). To validate the gradient expression pattern revealed by the spatial data analyses, RNA *in situ* and immunostaining with these gradient markers *Nefh* and Calb2 were performed. *Nefh* mRNAs are most abundantly detected at the basal region, less at the middle, and very weak at the apical region (Fig. 4d-g). Calb2 antibody immunostaining also displayed similar pattern, but the variation of gradient was not as sharp as *Nefh* (Fig. 4d-g). However, Calb2 gradients were obvious at E17.5 and adulthood (Fig. 3d). Note that *Nefh* expression pattern was reversed between E17.5 and P8 stage. The expression pattern of Calb2 was also changed, either temporally or spatially. Interestingly, *Nefh* expression gradient was reversed again in adulthood (Fig. S4d-f). Similarly, two distinct expression gradients were clearly observed from the differential gene expression analyses and direct spatial painting (Fig. S4e, f). Furthermore, according to SGN markers from the published data [24, 26, 33], three subtypes of neurons were annotated in the three regions respectively (Fig. 4e-g). *Nefh* was commonly expressed in all SGN subtypes but higher expressed in subtype III [33]. The relative higher expression of *Nefh* in basal region suggested that SGN subtype III may be predominantly located at the basal region. The temporal and spatial dynamics of neuronal gene gradients revealed

the progress of SGN development, differentiation and maturation.

Spatiotemporal profiling of the organ of Corti development

The organ of Corti (OC) is a specialized sensory structure located in the cochlea of the inner ear, playing a crucial role in hearing. The OC is embedded in the cochlear duct and rests on the basilar membrane, allowing it to be finely tuned to different frequencies of sound [40]. The spatial illustration of OC single-cell atlas revealed the spatial arrangement of different cell types within the cochlea, highlighting the specific localization of these cells (Fig. 5a). UMAP clustering demonstrates distinct cell types, including inner and outer hair cells, Deiter cells, pillar cells, Hensen's cells, tympanic border cells and inner sulcus cells (Fig. 5b). These cell types were colored according to their identity, emphasizing their unique spatial distribution (Fig. 5a). Specific marker genes such as *Otoa*, *Rspo2*, *Aqp4*, and *Ocm* were used for distinguishing these cell types. For example, *Otoa* is predominantly expressed in interdental cells, while *Ocm* is more highly expressed in the Outer hair cells (Fig. 5c). A UMAP plot from our previous single-nucleus transcriptomic dataset [33] illustrates the clustering of different cell types in the inner ear based on gene expression profiles (Fig. S5a). The OC cells are grouped into distinct clusters, including Claudin/Inner sulcus cells, outer sulcus cells, pillar cells, tympanic border cells, and hair cells (IHC, OHC). These clusters reflect the known cellular heterogeneity of the cochlea, confirming the specificity of the spatial single-cell transcriptome data analyses. The expression profiling of key marker genes across various identified cell clusters in our previous snRNA-seq dataset (Fig. S5b, c), consistent with the spatial transcriptomics findings (Fig. 5c, S5d), reinforcing the

identification of these cell types. Overall, the consistent patterns observed between spatial transcriptomics and single-cell RNA-seq data confirm the accuracy of cell type identification and their respective marker genes, providing a comprehensive view of cochlear cell diversity.

To further understand the changes of expression pattern occurring in the process of hair cell maturing, we fitted a master tree for hair cells from three stages in diffusion space. The tip of a branch enriched in E17.5 cells was selected as a root, and the proposed time was subsequently calculated as the distance of this root in the tree. The tree was then represented as a dendrogram that reproduced a branching trajectory based on the transcriptional similarity of the proposed time-ordered cells (Fig. S5e). The generated tree accurately reflects the developmental stage branching characteristics. Dynamic gene expression changes during these three developmental stages were demonstrated by heatmaps, with genes such as *Ocm*, *Apod*, *Ptgds* and *Nnat*, displaying distinct temporal expression patterns (Fig. S5f). Highlighting the average expression of key marker genes, *Tectb*, *Nnat*, *Apod*, and *Ocm* showed dynamic changes from E17.5 to adulthood, further validating transcriptional changes in cochlear development (Fig. S5h). The proposed temporal trajectories of key genes were demonstrated, illustrating the dynamics of cellular expression during developmental stages (Fig. S5g). *Ocm*, *Apod*, *Nnat*, and *Tectb* peaked in expression during different developmental windows, reflecting their roles in hair cell maturation. Overall, this analysis provides insights into the spatial and temporal gene expression profiles within the OC, revealing key molecular changes that accompany the maturation of cochlear cell types and supporting

structures critical for hearing function.

Developmental dynamics and Spatial patterning of cochlear hair cells

The whole amount Myo7a immunostaining of cochlear epithelia demonstrated the temporal and spatial dynamics of hair cells at different stages. The hair cells are well defined around E16.5 stage following a basal-to-apical gradient [41]. All the hair cells were well differentiated at E17.5, including the apical regions (Fig. 5d). The apical hair cells expressed relative weaker Myo7a. No significant differences of Myo7a signals between IHCs and OHCs from apex-to-base. At P7 stage, the Myo7a expression in apical region was clear and became stronger comparing to E17.5 cochlea, revealing further differentiation of hair cells in the apex. Relatively stronger expression of Myo7a in the middle region than in the apical and basal regions (Fig. 5e). In adulthood, the Myo7a expressions of IHCs display an averaged pattern from apex-to-base, relatively slightly higher in apical region (Fig. 5f, g). While the Myo7a expression in OHCs showed a huge divergence from apex-to-base (Fig. 5f, g). The basal OHCs express very low level of Myo7a (Fig. 5g). Note the sharp contrast of Myo7a signals between IHCs and OHCs in the apical region (Fig. 5g). At the middle region, the expression Myo7a was gradually increased in OHCs following a basal-to-apical gradient (Fig. 5g). The Myo7a signals between OHCs and IHCs show less divergence along the gradient and became no significant divergence at the apex (Fig. 5f).

To further validate this expression gradient in OHCs, all the hair cells were extracted from the spatial single-cell atlas to analyze the spatial differentially expressed genes (DEGs) (Fig. 6a and S6-1a-d). After pairwise comparisons of OHC, a large

number of spatial DEGs were isolated from E17.5 (Fig. S6-1b, Table S3), P8 (Fig. S6-1d, Table S3), and adulthood (Fig. 6b, Table S3). After filtering for p-values < 0.05 and intersecting with a dataset of HC-specific genes (Table S1), 184, 265, and 205 genes were retained for the three datasets, respectively. There are two patterns of gene expression gradients for these spatial DEGs. In adulthood, genes like *Myo7a*, *Asb1*, and *Cachd1* displayed a decrease gradient from apical to basal pattern, whereas genes *Fat2*, *Fam83f*, and *Cab39* showed a reversed gradient (Fig. 6b). These spatial DEG data, particularly the *Myo7a* gene, are well matched with the whole amount Myo7a immunostaining results (Fig. 5f, g). Immunostaining of Myo7a on adult cochlear sections was performed for further confirmation of this gradient pattern (Fig. 6c). The OHCs at the apical regions show comparable Myo7a signal intensity with IHC, while the Myo7a expression is relatively lower than the IHCs in the basal region (Fig. 5f, g and 6c). But this Myo7a gradient was dynamic and only established in adulthood. At P8 stage, the apical OHCs expressed low level of Myo7a, comparing to the apical IHCs or middle OHCs (Fig. S6-1d-f). The immunostaining results are consistent with the differential expression results (Fig. S6-1d-f), revealing the value of these spatial data and the accuracy of data analyses.

Spatiotemporal dynamics of communication between hair cells and SGNs reveal the tonotopic organization along cochlear axis

To understand how hair cells cooperate with neuron cells to sense and convey different-frequency sound signals, we interrogated secreted signaling events among cochlear auditory epithelium and SGN for the three datasets. At E17.5 stage, the

maximum number of interactions is between neuron and hair cell, when the SGNs are the hub (Fig. S7-1a, b). This result is consistent with core function of SGNs for receiving the signals from HCs. Whereas, the stronger communications are between supporting cell subtypes and HC when the HCs are the hubs (Fig. S7-1b, right). It revealed that HCs communicate with nearby supporting cell types to coordinate its sensory function, not only just connecting with SGNs. These data also revealed that HCs are the center of cell communications in cochlea. At P8 stage, the number of interactions increased, either between SGNs and HCs or other cell types (Fig. 7b). As for hair cell, the strength of interaction with neighbor cells like inner sulcus cell and interdental cell (lateral kolliker's organ), as well as Hensen's cell became stronger (Fig. 7b, S7-1b). Next, all pathways were analyzed and ranked according to these spatial single cell atlas data. The interaction strength of Ptn-Sdc, Mdk-sdc, and Fgf pathways are among the top 3 of all the interactions (Fig. S7-2). Fgf signaling pathway plays crucial roles in inner ear development [42]. These pathways were further analyzed between these cell types of OC. When neuron cell acted as the signaling source, it interacted with cells from the OC mainly by Fgf10-Fgfr2 signaling both at E17.5 and P8 stages (Fig. 7c, S7-1c). When hair cell acted as the signaling source at P8, it mainly interacted with other cells from the OC by Fgf8-Fgfr2 signaling, especially with Deiter cell/pillar cell (Fig. 7c). While hair cell mainly interacted with other cells by Fgf10-Fgfr1 (Fig. 7c). With RNAscope assay, the expression location of *Fgf10* and *Fgfr2* were confirmed, which was largely consistent with spatial expression result (Fig. 7e, f).

Regionalized cell communications were further analyzed by utilizing the

advantages of spatial transcriptomic data. The OC cell types from apical, middle, and basal regions were extracted from the whole spatial single-cell atlas, and were subjected to differential cell communication studies. The overall cell communications were weak at the apical region, but relatively stronger in the middle and basal regions (Fig. 8a-c). The results showed that the strongest communications are found in the middle region (Fig. 8b). Obvious variations of the connection intensity between SGNs and HCs were shown among these three different regions (Fig. 8a-c). The apical region displayed the weakest connecting intensity while the middle and basal regions showed the strongest connection (Fig. 8a-c). Tuj1, also known as βIII-tubulin, is a widely recognized marker for neuronal cells [43] and is often used for detecting the neuronal projections of SGNs in the inner ear [44, 45]. The immunostaining of Tuj1 revealed that strongest signal intensity in the middle region rather than the apical and basal regions (Fig. 8d, e), suggesting their strong connections in the middle region. The projection features of SGNs revealed by immunostaining in three different regions was consistent with the differential communication studies (Fig. 8).

In this study, the spatiotemporal transcriptomic analyses reveal the developmental dynamics of HC and SGN, demonstrated their gradient gene expression pattern from apex-to-base, and their regionalized communications as well. These spatiotemporal data provided deeper insights into the molecular and cellular mechanism underlying the tonotopic organization along cochlear axis. According to these results, a model was proposed to illustrate the underlying mechanism for tonotopic organization (Fig. 8f). The cochlea organized its cell types in a spatially specific manner. The HCs and SGNs

expressed their relevant genes in a gradient pattern from apex to basal, either in a decreased or increased manner. Accordingly, their communications are toned into a spatially regionalized pattern. These variant gradients may be the molecular fundamentals for establishing the tonotopic organization.

Discussion

In this study, we performed spatial transcriptomic sequencing of the inner ear at various developmental stages, creating a single-cell resolution atlas of the cochlea that includes detailed spatial gene expression data. This approach enhances traditional tissue section RNAScope assays by enabling the examination of spatial expression profiles across different developmental stages and specific cell types. Due to the inherent limitations of the spatial technology itself, spatial transcriptomics still has some intrinsic issues that are difficult to resolve [27, 46]. The spatial stacking between cells is unavoidable and the thickness of cell bodies left in a tissue section is also spatially dynamic, which can all compromise the resolution and accuracy of spatial transcriptomics. Despite less resolution compared to routine single-cell approaches, the single-cell atlas established by spatial transcriptomic data is still useful for regular single-cell level analyses. This spatial dataset serves a valuable resource for researchers investigating inner ear development and auditory function, allowing for exploration of spatiotemporal gene expression patterns of any gene of interest, or any particular regions of interest.

Given the structural complexity of the inner ear, spatial information is crucial. Genetic variations affecting its morphology often result in hearing defect [47, 48].

While single-cell RNA-seq has been widely used in inner ear development research and has yielded a wealth of insights into inner ear development, it lacks the crucial spatial context essential for understanding developmental and genetic mechanisms. In contrast, our spatial transcriptomic analysis preserves this spatial context, providing significant advantages for studying inner ear development and architecture. Our spatial transcriptomic analysis offers invaluable insights that address these challenges and will undoubtedly have significant implications for the field. We mapped the expression patterns of known deafness-associated genes on inner ear tissue, revealing spatial expression hotspots that identify structures most vulnerable to mutations causing hearing loss (Fig. S8). These spatial data offer important resources for the fundamental studies on inner ear development, the discovery of deafness-causing genes, and the pathogenic mechanisms underlying hearing defects.

Our analyses identified distinct spatial expression patterns of spiral ganglion neurons (SGNs) subtype marker genes, suggesting significant spatial differentiation along the cochlear axis. This differentiation aligns with the established tonotopic organization of sound frequency perception. Although previous studies have revealed SGN heterogeneity and spatial gradients [10, 49], comprehensive molecular evidences supporting this tonotopic organization is lacking. SGNs are known to consist of Type I and Type II neurons, with Type I further subdivided into Ia, Ib, and Ic [24, 26]. Our previous work newly identified an additional SGN subtype, Type III [33], which is very similar with Type I SGNs according to their commonly expressed marker genes. The Type III marker gene *Nefh* displayed a significant gradient from base to apex of cochlea,

with high expression predominantly in basal regions (Fig. 4). A recent study using conventional immunostaining demonstrated differential distribution of SGN subtypes along the cochlear axis, with Type Ia and Ib neurons are primarily in apical and middle regions, while Type Ic is more concentrated in the base [10]. Our data corroborate these findings, with several type I or III SGN markers showing gradient distribution (Fig. 4, S4). The similarities in molecular features among subtype Ia, Ib, Ic, and III suggest that they may represent variations of Type I SGNs across different cochlea regions. Type III SGNs, predominantly found in the basal region (Fig. 4), may represent a new subtype of Type I SGNs, akin to subtype Ic [10]. The type III SGNs were not identified in previous studies likely due to the reasons that previous single-cell level transcriptomic analyses are performed by different approaches (scRNA-seq or snRNA-seq) and at different developmental stages (developmental or adult stages) [13, 24, 26]. The loss of spatial information might be an additional reason. Traditional histological and immunostaining methods are limited in their ability to achieve comprehensive large-scale molecular characterization and differential expression analysis of SGN subtypes [10]. The close molecular characteristics of Type I and III SGNs complicate their distinguishing. Our spatial data indicate that these subtypes may represent the same cell type (type I) exhibiting subtle molecular differences based on their spatial location along the cochlear axis, contributing to tonotopic organization [10, 33].

In addition to SGNs, outer hair cells (OHCs) also exhibit spatial gradient along the cochlear axis. While cochlear hair cells are classified into inner hair cells (IHCs) and OHCs, our findings reveal significant differences between OHCs located in the

basal and apical regions. Classic markers like *Myo7a* show a pronounced gradient from apex to base, indicating distinct molecular identities. Other proteins, including *Prestin* (Fig. S6-2), *Calb2*, *Kcnq4* and BK channels, were also reported to display gradient distributions [9] . Despite some inconsistences due to limited hair cell numbers in our spatial dataset, many reported gradient genes were confirmed. These findings suggest that OHCs may also subdivided into spatially distinct subtypes, similar to SGN subtypes, although further profiling is needed due to the limited number of captured hair cells.

Our spatial transcriptomic analysis also uncovered numerous other genes exhibiting gradient expression patterns along the cochlear axis, indicating that these gradients may contribute to the regional specialization or patterning of frequency sensitivity in the cochlea. Furthermore, our data revealed region-specific differences in cell-cell communication and connectivity within the cochlea, emphasizing the importance of regionalization in the inner ear's functional organization. Understanding these localized interactions is crucial for uncovering the mechanisms governing cochlear development and its ability to perceive sound frequencies with high precision. Overall, our study highlights the temporal and regionalized gene expression patterns, along with the specialized organization and communication among cell types, including hair cells, SGNs, and supporting cells. This coordinated mechanism is essential for establishing tonotopic patterning during development and achieving precise sensory function.

Methods

Animal and tissue collection

Wild-type C57BL/6 mice were bred in the laboratory. All animal experiments were conducted with approval from the Animal Research and Ethics Committee of the Chengdu Institute of Biology, Chinese Academy of Sciences (Approval No. CIBDWLL2018030). For E17.5 cochlear tissue, a pregnant female was euthanized and inner ears were dissected from pups. For postnatal time points, P8 and Adult mouse were euthanized and inner ears were dissected. Cochlea were separated from the inner ears under the stereo microscope (Olympus, SZ61) and washed by ice-cold DPBS. After wiping the liquid by dust-free paper, cochleae were rinsed with ice-cold OCT, and next moved into Cassettes with ice-cold OCT. In order to gain better longitudinal section with at least 4 cochlea duct regions, the tissue position in the cassette was fine-tuned under the stereo microscope again. Then the cassettes were quickly put on the dry ice to ensure the tissues were froze immediately. All samples were sent to Beijing Biomarker Technologies Co. the same day.

Tissue cryosection and processing for spatial-seq

The spatial-seq was performed with the BMKMANU S1000 Gene Expression kit (BMKMANU, ST03002). Tissue sectioning, RNA quality, HE staining, imaging and tissue optimization were followed by the BMKMANU S1000 Tissue Optimization kits user guide (BMKMANU, ST03003). The Cryosections were cut at a thickness of 10 μm and every section would be checked with HE staining before target structure section appearing. When 4 cochlea duct holes were observed, the next section would be moved

to slide for later sequencing.

Library preparation and sequencing

Library constructions were also performed according to the BMKMANU S1000 Library Construction Kit User Guide. The Illumina library was sequenced with Illumina NavoSeq 6000. The raw data from Illumina and Nanopore were mapped to the mouse reference genome (GRCm38, ftp://ftp.ensembl.org/pub/release-74/fasta/mus_musculus/) by BSTMatrix v2.4 (http://www.bmkmanu.com/wp-content/uploads/2024/07/BSTMatrix_v2.4.f.1.zip) and BSTMatrix-ONT v1.2 (http://www.bmkmanu.com/wp-content/uploads/2023/03/BSTMatrix-ONT_v1.2.zip), respectively, using default parameters. The image adjusted by BSTViewer V4.7 (http://www.bmkmanu.com/wp-content/uploads/2024/07/BSTViewer-V4.7.4.1.rar) and corresponding level 2 (10 μm) matrix were used for downstream analysis.

Cell clustering and cell-type identification

Downstream analysis of BSTViewer output data was performed using the R package Seurat (v5.1.0) (https://github.com/satijalab/seurat) [50]. HE images from the same sample were pooled together as a data set for analysis. First, for all samples, data was preliminary filtered with min.cell at 5 and min.fearture at 100, when imported into R. Then all datasets were normalized (scale.factor=10000) and scaled using all genes. Principal component analysis (PCA) focusing on the most variable features was performed and for all data, the first 30 dimensions obtained by RunPCA were applied to the analysis of RunUMAP, FindNeighbors, and FindClusters to obtain UMAP and cluster information. Cluster specific genes were identified by FindAllMarkers

differential expression analysis. Combining cell-type specific markers identified by Seurat and previously reported markers, spot' ident was annotated.

Cell communication analysis of hair cells and supporting cells

Cellchat (v1.6.1)[51] package was applied to explore the potential interaction pattern of cell types from OC and SGN. Based on the normalized gene-expression matrix of our datasets, the database of mouse ligand-receptor interactions was used to identify overexpressed genes and interactions with the method of "trimean", compute the communications and related pathways. All analysis steps were followed by the suggested workflow of CellChat with the default parameters.

Pseudotime trajectory analysis of HC and SGN groups

The newCellDataSet function of Monocle2 (2.32.0) [52] was utilized to create a CellDataSet object, and the estimateSizeFactors and estimateDispersions functions were applied for the estimation of size factors and dispersions, respectively. By employing the detectGenes function, genes expressed in at least 10 cells were identified, and key genes for trajectory inference were set using the setOrderingFilter function. Subsequently, the reduceDimension and orderCells functions were applied for dimensionality reduction and cell ordering to construct the pseudotime trajectory of cells. The plot_cell_trajectory function was used to visualize the cellular trajectories, which were colored according to cell states. Additionally, genes with expression changes during cell development and genes that regulate the branching points of cellular differentiation were identified using the differentialGeneTest and BEAM functions. Finally, a heatmap of pseudotime-associated genes was generated using the

plot_pseudotime_heatmap function to display the expression patterns of these genes across different cellular states.

Gene expression pattern analysis from apex to basal part

To explore regional gene-expression characteristics along the cochlea duct, the expression matrixes of SGN and organ of Corti cell types from apex, middle-basal and basal reagions (Fig. 4a; Fig S4a and d) were extracted separately for DEG analysis, with the method of wilcoxon test. To better reveal the expression pattern of differential genes, plot_density method from Nebulosa (V1.14) package[53] was used to depict spatial expression.

Immunofluorescence

Cochleae from E17.5, P8 and Adult mice were fixed in 4% paraformaldehyde diluted in 1×PBS for 2 hours at 4 ℃, washed in 1×PBS for three times, dehydrated by 30% sucrose solution, then embedded in OCT Compound for cryosectioning at 10 μm thickness. According to previous publications [54], the immunofluorescence was performed as following steps. Briefly, sections were blocked in 5% bovine serum albumin (BSA, Biofroxx, 1110GR500)/10% horse serum albumin (HSA, Sangon Biotech, E510006-0100) / 0.5% Triton-X/1×PBS for 8~10 hours at 4 ℃ and primary antibodies were applied overnight at 4 ℃ in 5% BSA/10% HSA/0.5% Triton-X/1×PBS. All antibodies used were list in Table S1. Secondary antibodies were applied in 5% BSA/10% HSA/0.5% Triton-X/1×PBS for 6~8 hours at 4 ℃ followed by DAPI nuclear staining. All washes following primary and secondary antibody application were performed with 1% Triton-X/1×PBS. All fluorescent images were acquired using

fluorescent microscope system (Nikon, Eclipse 55i). All antibody used in this study were listed in Table S4.

RNA *in situ* hybridization

The fragments of target genes (Table S4) were prepared by PCR amplification of cDNA from cochleae RNA, with reverse primers containing a T7 RNA polymerase promoter sequence. Next the DIG-labeled RNA probes were synthesized by the transcription reaction using Riboprobe Systerm-T7 kit (Promega, P1440) and DIG labeled UTP (Roche, 11277073910). The slides for RNA in situ hybridization (RNA-ISH) were prepared with the same steps of Immunohistochemistry. Then RNA-ISH was conducted as following steps, according to previous publications [33, 55]. Firstly, slides were fixed by 4% PFA for 5 min at RT and washed in 1×PBS for 3 min and in distilled water for 1 min. Next for permeabilizing, slides were immersed in 0.2 M HCl for 15 min and 0.1 M triethanolamine-HCl for 10 min. After being washed in 1×PBS for 5 min, slides were dehydrated by washing for 20 min per wash in 70%, 85% and 100% ethanol. And then slides were treated by hybridization buffer containing DIG-labeled RNA probes overnight at 65 ℃. To remove non-specific and repetitive RNA hybridization, slides were washed in 5×saline sodium citrate (SSC) for 5 min at RT and 2×SSC for 30 min at 60 ℃. After being treated in 0.3% H_2O_2 for 1 h at RT, slides were blocked for 2 h at RT and next incubated with anti-DIG antibody overnight at 4 ℃. Finally, the signal was detected by the TSA® Plus Cyanine 3.5 (Cy3.5) detection kit (NEL763001KT, Akoya) and slides were sealed by diluted DAPI with glycerin. The images were captured by fluorescent microscope.

Statistical analysis

All statistical analyses were conducted by R and RStudio. And as for the results of wilcoxon-test, which were used to uncover the spatial differential expression genes for neuron cell and OHC, P-value < 0.05 were considered statistically significant.

Conflicts of interest

The authors declared no competing interests.

Data availability

The raw sequence data generated in this paper have been deposited in the Genome Sequence Archive [56] in National Genomics Data Center [57], China National Center for Bioinformation, Beijing Institute of Genomics, Chinese Academy of Sciences (GSA: CRA019653) that are publicly accessible at https://ngdc.cncb.ac.cn/gsa. The ChIP-seq data of mouse inner ear from The mouse inner ear single-cell RNA-seq data at adult stage from our publication [33] have been deposited and can be accessible in the National Genomics Data Center under the number (CRA015540). The E17.5 and P8 single-cell RNA-seq data used for integration study were accessed under the number GSE137299 from previous publications [17, 18].

Acknowledgments

The work was supported by the National Natural Science Foundation of China (Nos.

82300142, 82301316, 32370882, and 32370536), and the Central Government Guides Local Science and Technology Development Funds in Sichuan Provincial (2022ZYD0131), and the Fundamental Research Funds for the Central Universities (BMU2021YJ064). We gratefully acknowledge the High-performance Computing Platform of Peking University for conducting the bioinformatics analysis.

Author's contribution

J. Li, Y. Zhao, and H. Wu designed the work; M. Yan, P. Zhang, H. Wang, J.H. Li, Y. Wang, X. Zeng, and Y. Gao acquired the data; M. Yan, H. Wang, Y. Wang, B. Zhu, D. Deng, X. Guo, L. Ma and Y. Feng analyzed the data; M. Yan, Y. Wang, and H. Wang made the figures; J. Li, Y. Zhao, and H. Wu wrote the paper.

References

1. Groves, A.K. and D.M. Fekete, *Shaping sound in space: the regulation of inner ear patterning.* Development, 2012. **139**(2): p. 245-257.
2. Torres, M. and F. Giráldez, *The development of the vertebrate inner ear.* Mechanisms of development, 1998. **71**(1-2): p. 5-21.
3. Wu, D.K. and M.W. Kelley, *Molecular mechanisms of inner ear development.* Cold Spring Harbor perspectives in biology, 2012. **4**(8): p. a008409.
4. Whitfield, T.T., *Development of the inner ear.* Curr Opin Genet Dev, 2015. **32**: p. 112-8.
5. Roccio, M., P. Senn, and S. Heller, *Novel insights into inner ear development and regeneration for targeted hearing loss therapies.* Hearing research, 2020. **397**: p. 107859.
6. Toppila, E., et al., *Individual risk factors in the development of noise-induced hearing loss.* Noise and Health, 2000. **2**(8): p. 59-70.
7. Kujawa, S.G. and M.C. Liberman, *Translating animal models to human therapeutics in noise-induced and age-related hearing loss.* Hearing research, 2019. **377**: p. 44-52.
8. Meghji, S. and J. Phillips, *The significance of audiometric notching in individuals with a history of noise exposure: a systematic review.* Ear and Hearing, 2021. **42**(5): p. 1109-1118.
9. Mann, Z.F. and M.W. Kelley, *Development of tonotopy in the auditory periphery.* Hearing research, 2011. **276**(1-2): p. 2-15.
10. Wang, M., S. Lin, and R. Xie, *Apical-basal distribution of different subtypes of spiral ganglion*

neurons in the cochlea and the changes during aging. Plos one, 2023. **18**(10): p. e0292676.

11. Atkinson, P.J., et al., *Sensory hair cell development and regeneration: similarities and differences.* Development (Cambridge, England), 2015. **142**(9): p. 1561.
12. Ding, D., H. Jiang, and R.J. Salvi, *Mechanisms of rapid sensory hair-cell death following co-administration of gentamicin and ethacrynic acid.* Hearing research, 2010. **259**(1-2): p. 16-23.
13. Wang, S., et al., *3D reconstruction of the mouse cochlea from scRNA-seq data suggests morphogen-based principles in apex-to-base specification.* Dev Cell, 2024. **59**(12): p. 1538-1552 e6.
14. Tobin, M., et al., *Stiffness and tension gradients of the hair cell's tip-link complex in the mammalian cochlea.* eLife, 2019. **8**: p. e43473.
15. Ruan, Q., et al., *Topological and developmental expression gradients of Kir2. 1, an inward rectifier K+ channel, in spiral ganglion and cochlear hair cells of mouse inner ear.* Developmental neuroscience, 2009. **30**(6): p. 374-388.
16. Shi, T., et al., *Single-cell transcriptomic profiling of the zebrafish inner ear reveals molecularly distinct hair cell and supporting cell subtypes.* Elife, 2023. **12**: p. e82978.
17. Jean, P., et al., *Single-cell transcriptomic profiling of the mouse cochlea: An atlas for targeted therapies.* Proceedings of the National Academy of Sciences, 2023. **120**(26): p. e2221744120.
18. Kolla, L., et al., *Characterization of the development of the mouse cochlear epithelium at the single cell level.* Nature communications, 2020. **11**(1): p. 2389.
19. Sun, G., et al., *Single-cell transcriptomic atlas of mouse cochlear aging.* Protein & Cell, 2023. **14**(3): p. 180-201.
20. Milon, B., et al., *A cell-type-specific atlas of the inner ear transcriptional response to acoustic trauma.* Cell reports, 2021. **36**(13).
21. Benkafadar, N., et al., *Transcriptomic characterization of dying hair cells in the avian cochlea.* Cell reports, 2021. **34**(12).
22. Janesick, A.S., et al., *Avian auditory hair cell regeneration is accompanied by JAK/STAT-dependent expression of immune-related genes in supporting cells.* Development, 2022. **149**(8).
23. Baek, S., et al., *Single-cell transcriptome analysis reveals three sequential phases of gene expression during zebrafish sensory hair cell regeneration.* Developmental cell, 2022. **57**(6): p. 799-819. e6.
24. Shrestha, B.R., et al., *Sensory Neuron Diversity in the Inner Ear Is Shaped by Activity.* Cell, 2018. **174**(5): p. 1229-1246 e17.
25. Petitpré, C., et al., *Single-cell RNA-sequencing analysis of the developing mouse inner ear identifies molecular logic of auditory neuron diversification.* Nature communications, 2022. **13**(1): p. 3878.
26. Sun, S., et al., *Hair cell mechanotransduction regulates spontaneous activity and spiral ganglion subtype specification in the auditory system.* Cell, 2018. **174**(5): p. 1247-1263. e15.
27. Longo, S.K., et al., *Integrating single-cell and spatial transcriptomics to elucidate intercellular tissue dynamics.* Nature Reviews Genetics, 2021. **22**(10): p. 627-644.
28. Piwecka, M., N. Rajewsky, and A. Rybak-Wolf, *Single-cell and spatial transcriptomics: deciphering brain complexity in health and disease.* Nature Reviews Neurology, 2023. **19**(6): p. 346-362.
29. Asp, M., et al., *A spatiotemporal organ-wide gene expression and cell atlas of the developing human heart.* Cell, 2019. **179**(7): p. 1647-1660. e19.

30. Farah, E.N., et al., *Spatially organized cellular communities form the developing human heart.* Nature, 2024. **627**(8005): p. 854-864.
31. Yao, Z., et al., *A high-resolution transcriptomic and spatial atlas of cell types in the whole mouse brain.* Nature, 2023. **624**(7991): p. 317-332.
32. Kanemaru, K., et al., *Spatially resolved multiomics of human cardiac niches.* Nature, 2023. **619**(7971): p. 801-810.
33. Li, J., *Single-cell atlas comparison across vertebrates reveals evolution of auditory cell types and mechanisms for hair cell regeneration.* 2024.
34. Peeleman, N., et al., *On the Role of Fibrocytes and the Extracellular Matrix in the Physiology and Pathophysiology of the Spiral Ligament.* Frontiers in Neurology, 2020. **11**.
35. Petitpre, C., et al., *Single-cell RNA-sequencing analysis of the developing mouse inner ear identifies molecular logic of auditory neuron diversification.* Nat Commun, 2022. **13**(1): p. 3878.
36. Sun, G., et al., *Single-cell transcriptomic atlas of mouse cochlear aging.* Protein Cell, 2023. **14**(3): p. 180-201.
37. Petitpré, C., et al., *Neuronal heterogeneity and stereotyped connectivity in the auditory afferent system.* Nature Communications, 2018. **9**(1).
38. Harlow, D.E., et al., *Expression of proteolipid protein gene in spinal cord stem cells and early oligodendrocyte progenitor cells is dispensable for normal cell migration and myelination.* Journal of Neuroscience, 2014. **34**(4): p. 1333-1343.
39. Chew, H., V.A. Solomon, and A.N. Fonteh, *Involvement of lipids in Alzheimer's disease pathology and potential therapies.* Frontiers in physiology, 2020. **11**: p. 598.
40. Rask-Andersen, H., et al., *Human cochlea: anatomical characteristics and their relevance for cochlear implantation.* The Anatomical Record: Advances in Integrative Anatomy and Evolutionary Biology, 2012. **295**(11): p. 1791-1811.
41. Chonko, K.T., et al., *Atoh1 directs hair cell differentiation and survival in the late embryonic mouse inner ear.* Developmental biology, 2013. **381**(2): p. 401-410.
42. Pirvola, U., et al., *FGF/FGFR-2 (IIIb) signaling is essential for inner ear morphogenesis.* Journal of Neuroscience, 2000. **20**(16): p. 6125-6134.
43. Guo, J., C. Walss-Bass, and R.F. Ludueña, *The β isotypes of tubulin in neuronal differentiation.* Cytoskeleton, 2010. **67**(7): p. 431-441.
44. Ahmed, M., J. Xu, and P.-X. Xu, *EYA1 and SIX1 drive the neuronal developmental program in cooperation with the SWI/SNF chromatin-remodeling complex and SOX2 in the mammalian inner ear.* Development, 2012. **139**(11): p. 1965-1977.
45. Breuskin, I., et al., *Glial but not neuronal development in the cochleo-vestibular ganglion requires Sox10.* Journal of neurochemistry, 2010. **114**(6): p. 1827-1839.
46. Gulati, G.S., et al., *Profiling cell identity and tissue architecture with single-cell and spatial transcriptomics.* Nature Reviews Molecular Cell Biology, 2024: p. 1-21.
47. Jiang, L., et al., *Advances in gene therapy hold promise for treating hereditary hearing loss.* Molecular Therapy, 2023. **31**(4): p. 934-950.
48. Sennaroğlu, L. and M.D. Bajin, *Classification and current management of inner ear malformations.* Balkan medical journal, 2017. **34**(5): p. 397-411.
49. Markowitz, A.L. and R. Kalluri, *Gradients in the biophysical properties of neonatal auditory neurons align with synaptic contact position and the intensity coding map of inner hair cells.* Elife, 2020. **9**: p. e55378.

50. Hao, Y., et al., *Dictionary learning for integrative, multimodal and scalable single-cell analysis.* Nat Biotechnol, 2024. **42**(2): p. 293-304.
51. Jin, S., et al., *Inference and analysis of cell-cell communication using CellChat.* Nature Communications, 2021. **12**(1).
52. Qiu, X., et al., *Reversed graph embedding resolves complex single-cell trajectories.* Nature Methods, 2017. **14**(10): p. 979-982.
53. Alquicira-Hernandez, J. and J.A.-O. Powell, *Nebulosa recovers single-cell gene expression signals by kernel density estimation.* Bioinformatics, 2021. **37**(16): p. 2485-2487.
54. Li, J., et al., *Dynamic changes in cis-regulatory occupancy by Six1 and its cooperative interactions with distinct cofactors drive lineage-specific gene expression programs during progressive differentiation of the auditory sensory epithelium.* Nucleic acids research, 2020. **48**(6): p. 2880-2896.
55. Sun, Y., et al., *Single-cell transcriptomic landscapes of the otic neuronal lineage at multiple early embryonic ages.* Cell Reports, 2022. **38**(12).
56. Chen, T., et al., *The genome sequence archive family: toward explosive data growth and diverse data types.* Genomics, Proteomics and Bioinformatics, 2021. **19**(4): p. 578-583.
57. *Database resources of the national genomics data center, China national center for bioinformation in 2022.* Nucleic Acids Research, 2022. **50**(D1): p. D27-D38.

Figure Legends

Figure 1

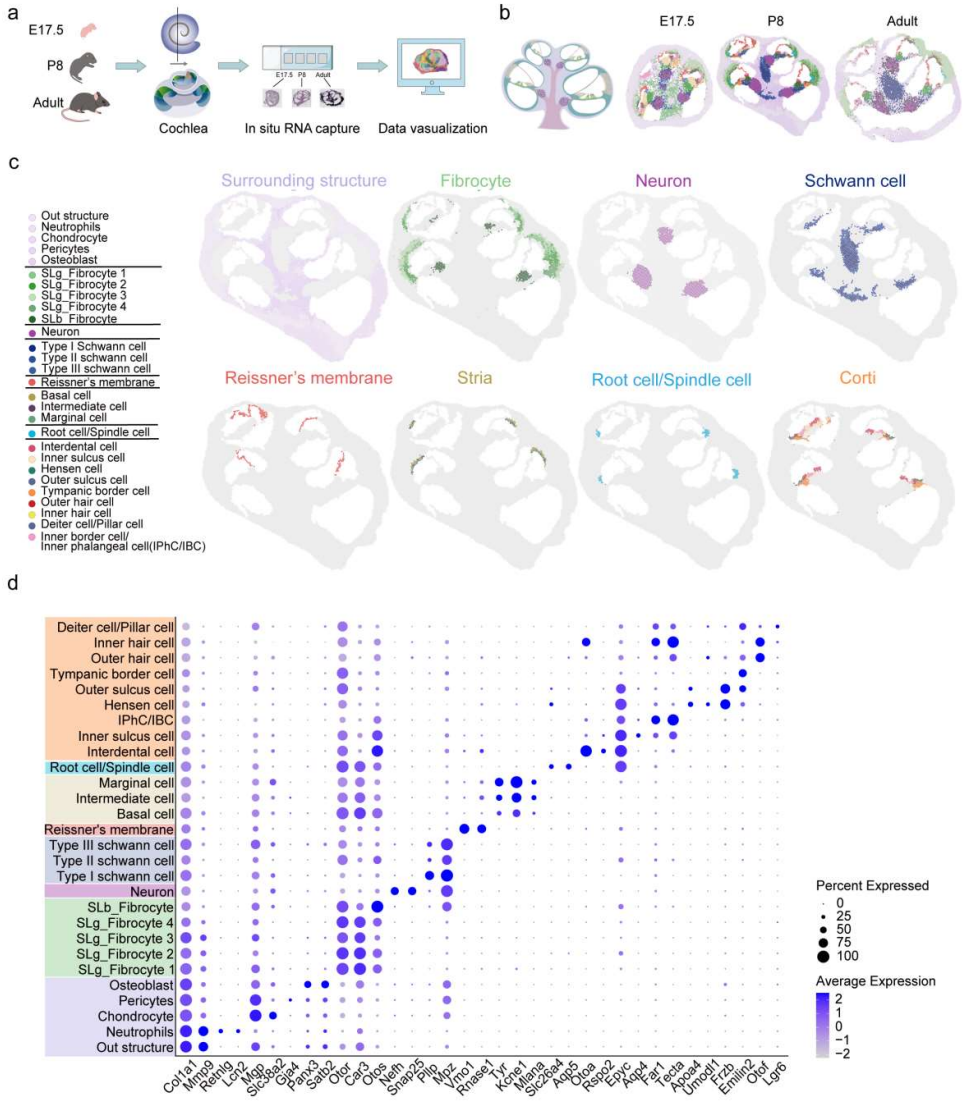

Fig. 1 Spatial single-cell atlas of developing and adult cochlea. (**a**) The work flow of spatial transcriptomic assay for mouse cochlea at three stages (E17.5, P8, 2M). (**b**) Left, the diagram of cochlea depicting the cross-section direction. Right, visualization of spatial RNA-seq barcoded spots colored by cell types for the three developmental stages. (**c**) Spatial single cell types in the P8 cochlea cross-section. Eight major groups

of cell types were shown, respectively SLg: spiral ligament, SLb: spiral limbus. (**d**) Bubble plot analysis of the top differentially expressed genes for each cell types in the P8 cochlea. The size of the dots represents the percentage of cells in the clusters expressing the genes and the color intensity represents the average expression levels of the gene in that cluster.

Figure 2

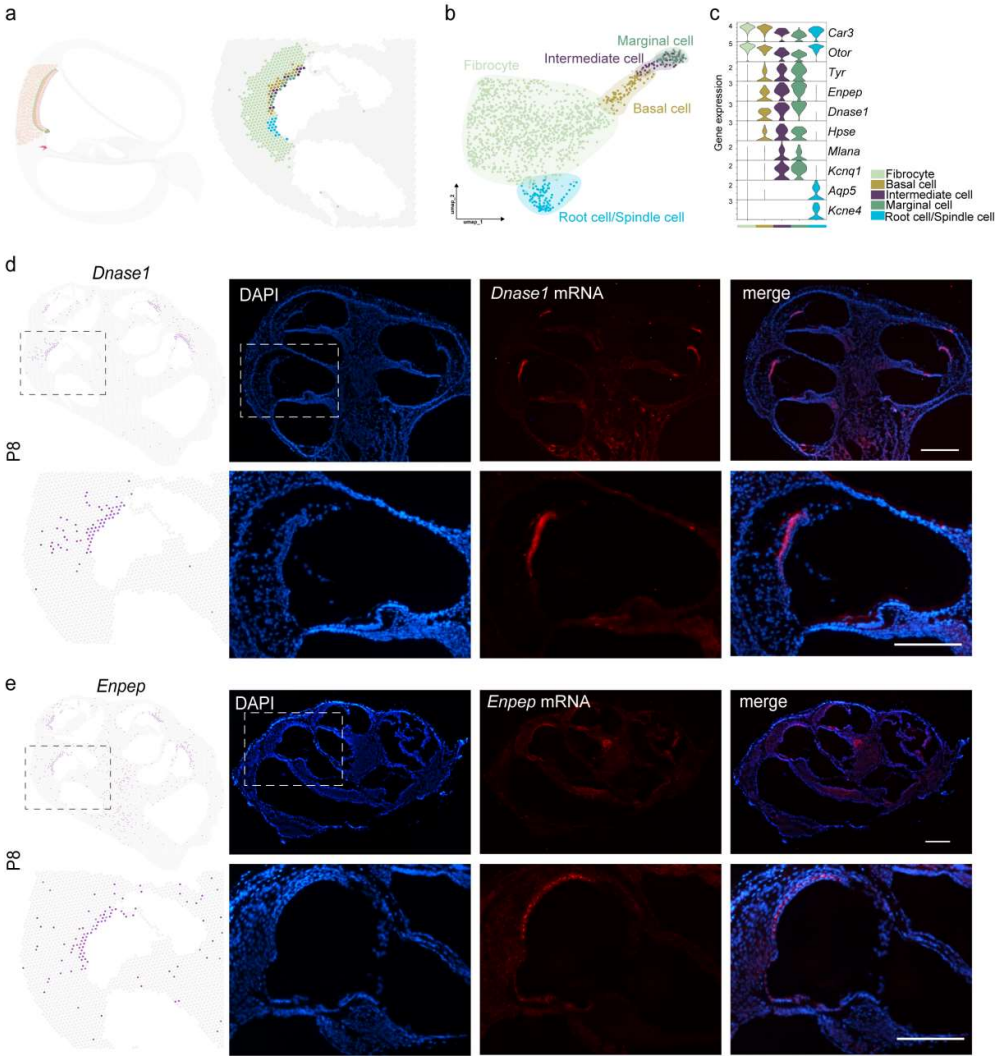

Fig. 2 Spatial analyses of lateral wall cell subtypes. (**a**) Left, the diagram of the cochlea highlighting main cell types from the lateral wall structure. Right, the spatial distribution of lateral wall cell subtypes at P8 cochlea. (**b**) UMAP plot showing the cell types in lateral wall (LW) in the P8 datasets. (**c**) Violin plots showing the differential expression genes to distinguish each LW cell type. (**d**) Upper, spatial dot painting for *Dnase1* gene expression on spatial chip and its RNA *in situ* detection on P8 whole-cochlea cryosection. The *Dnase1* mRNA signal is in red and DAPI is blue. Bottom,

magnified view of selected region above, as indicated by white dashed box above. (**e**) Upper, spatial painting of *Enpep* gene on chips and its RNA *in situ* validation on the P8 whole-cochlea cryosection. The *Enpep* mRNA signal is in red and DAPI is blue. Bottom, magnified view of selected region in above dashed box. All scale bar equals to 200 μm.

Figure 3

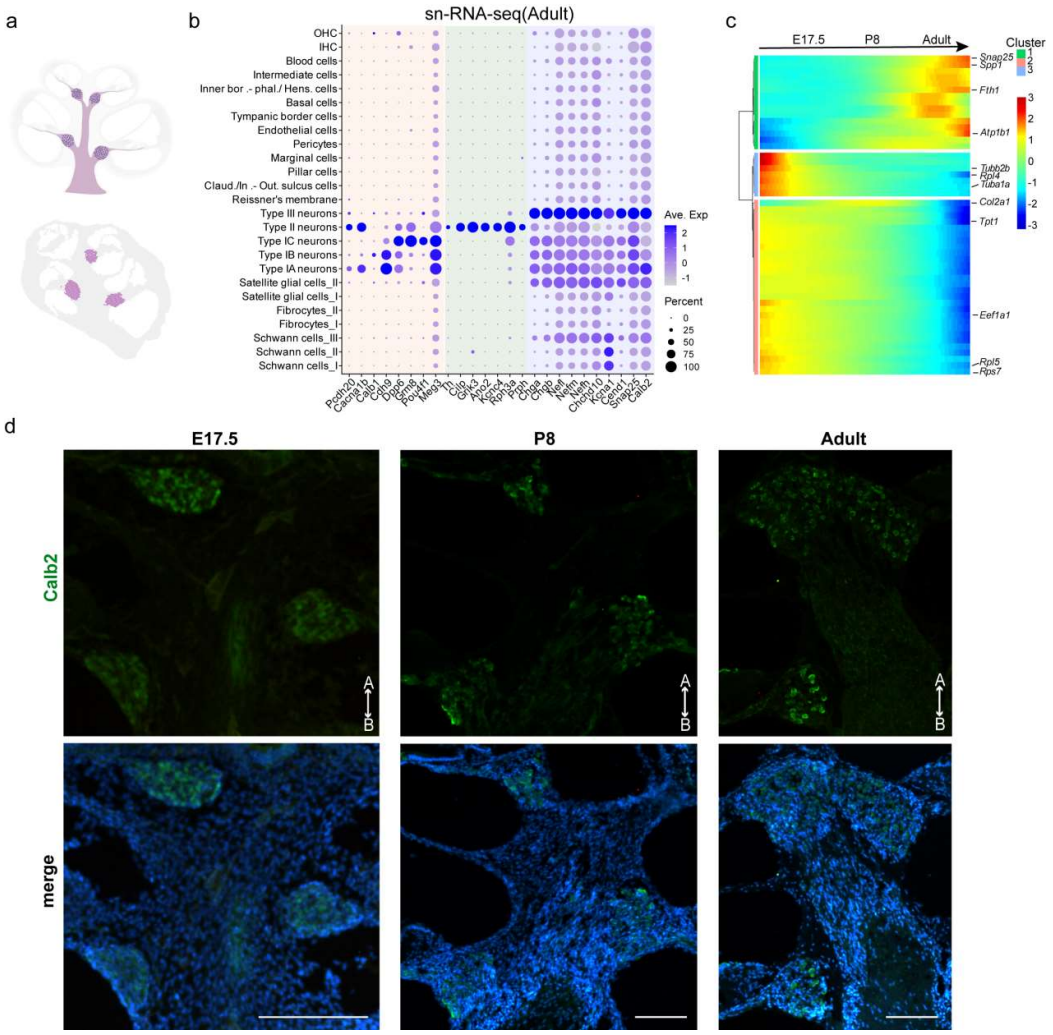

Fig. 3 Temporal dynamics of gene expression in spiral ganglion neurons during cochlear development. (**a**) Upper, the diagram of neuronal system in cross-section of cochlea. Bottom, the spatial distribution of neuron cells at P8 cochlea. (**b**) Bubble plot showing the differential expression of 25 neuron markers representing each SGN subtype identified in previous single-cell or single-nucleus RNA-seq dataset. OHC, outer hair cell IHC, inner hair cell; IPhC/IBC, inner phalangeal cell/inner border cell; ISC/OSC/CC, inner sulcus cell/outer sulcus cell/Claudius cell. The size of the dots represents the percentage of cells in the clusters expressing the genes and the color

intensity represents the average expression levels of the gene in that cluster. (**c**) Heatmap showing the pseudotime analysis for neuron cells from E17.5, P8 and adult dataset, with the top 10 upregulated genes along the differentiation of each branch. (**d**) Immunostaining of Calb2 on the E17.5, P8, adult cochlea cross-section. Calb2 is labeled in green and DAPI is blue. A, apex; B, base. Scale bar equals to 200 μm.

Figure 4

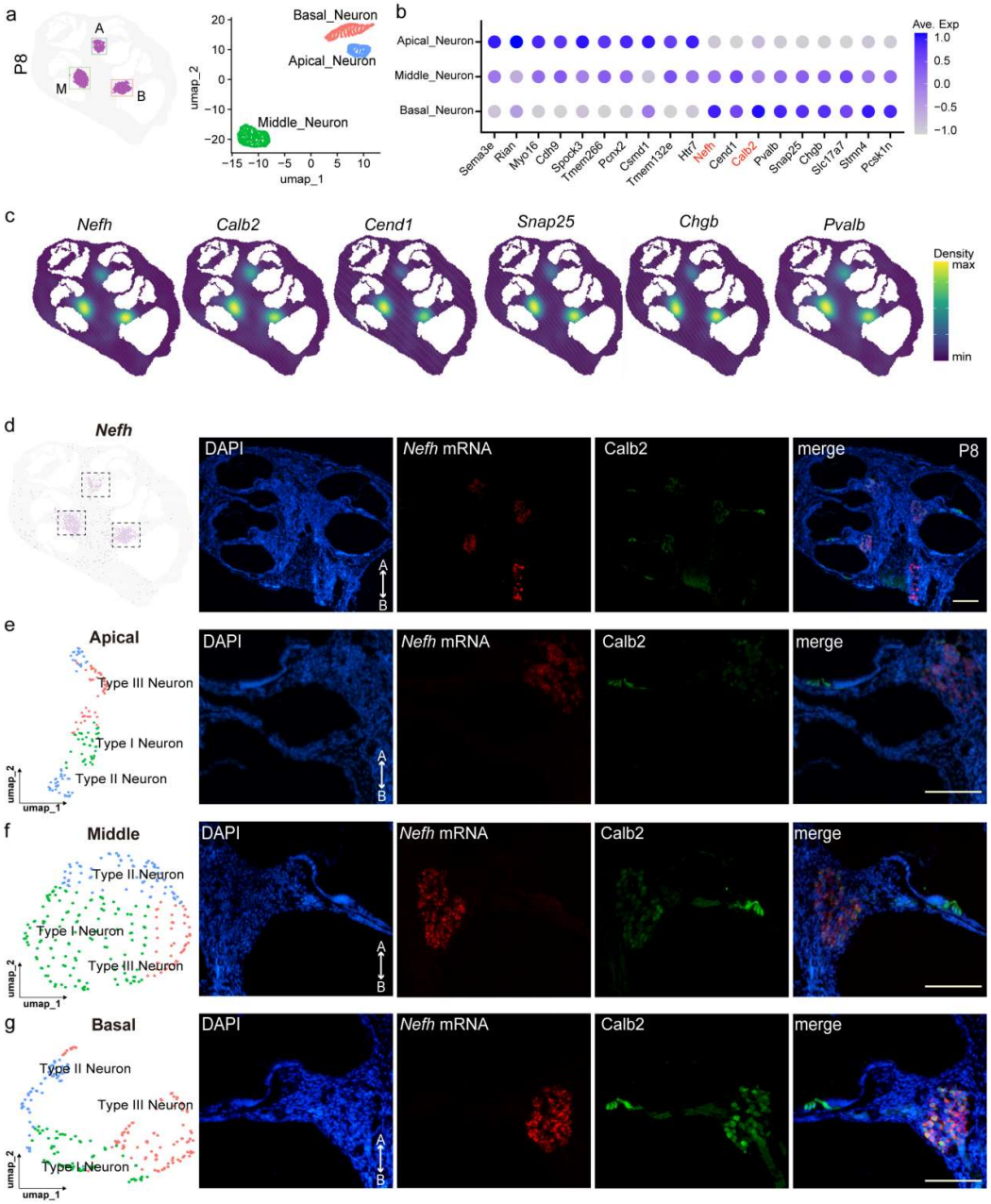

Fig. 4 Spatial differential analysis reveals gradients of neuronal gene expression from apical to basal SGNs. (**a**) Left, spatial painting of spiral ganglion neurons (SGNs) at P8 cochlea. The rectangular boxes with different colors indicate three different regions. A, apical; M, middle; B, basal. Right, UMAP plot showing the apical middle and basal neurons extracted from P8 cochlea in the left. (**b**) Bubble plot showing the

expression level of the 17 gradient genes representing two patterns (decreasing or increasing expression pattern from apex to base). The genes which were confirmed by RNA *in situ* or immunofluorescent staining assay were labeled in red. The size of the dots represents the percentage of cells in the clusters expressing the genes and the color intensity represents the average expression levels of the gene in that cluster. (**c**) Density plots showing the spatial expression of *Nefh*, *Calb2*, *Cend1*, *Snap25*, *Chgb* and *Pvalb*, on P8 cochlea section chip. (**d**) Left, spatial expression of *Nefh* on P8 cochlea section, black dotted boxes labeled the neuron cells from apical, middle, and basal region, respectively. Right, immunostaining of Calb2 (green) and RNA *in situ* detection of *Nefh* mRNA (red) on P8 cochlea cross-section. DAPI is in blue. (**e-g**) Left, UMAP plots showing the neuronal cell subtypes from apical, middle and basal region, respectively. Right, magnified view of neuron cell staining in apex region, middle and basal regions, respectively. All scale bar equals to 200 μm.

Figure 5

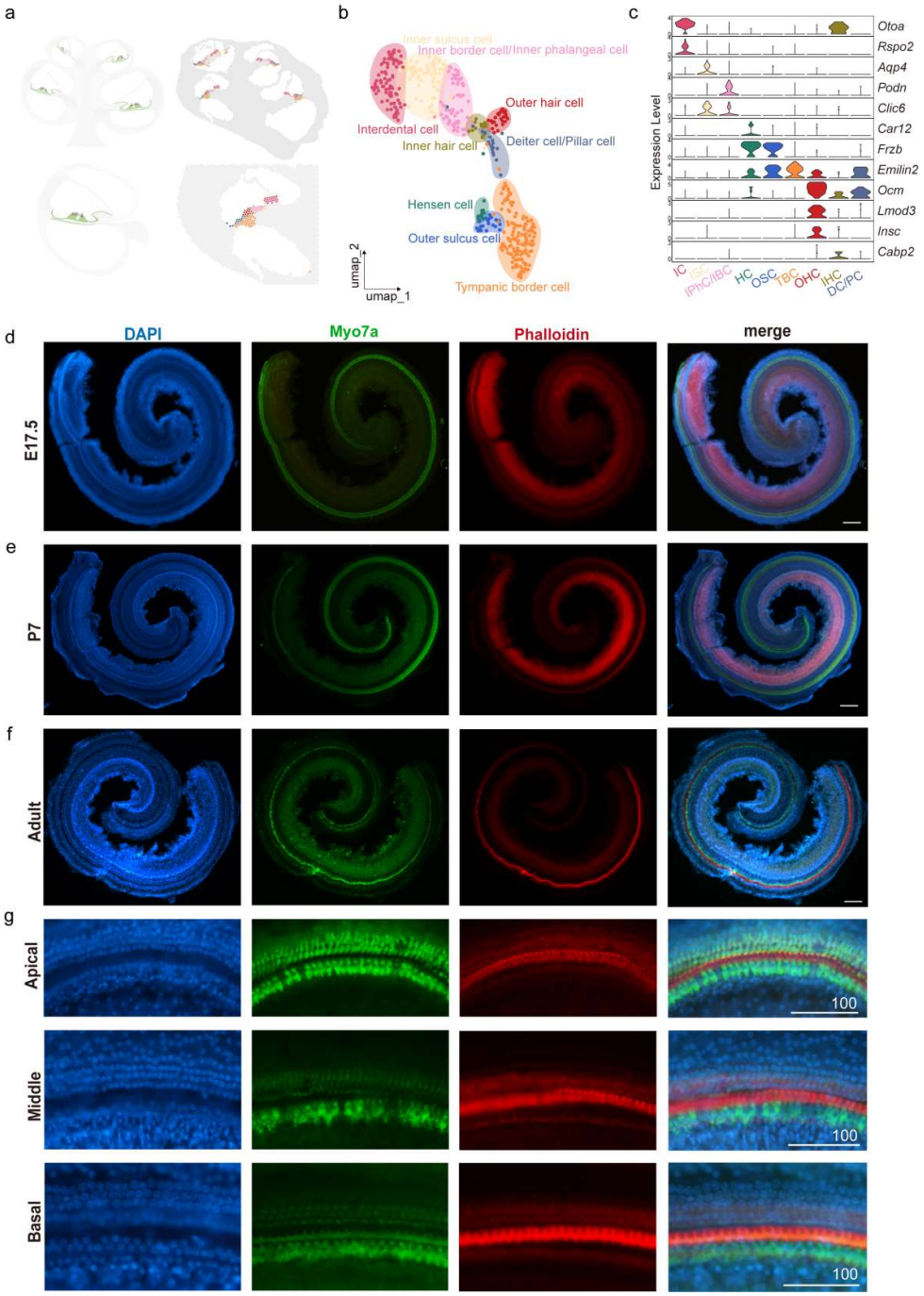

Fig. 5 Spatiotemporal analysis for the organ of Corti cell. (**a**) Upper left, the diagram of cochlea cross-section highlighting the cells from the organ of Corti (OC). Upper right, spatial painting of cell clusters from OC identified in P8 cochlea. Bottom left, magnified

view of (**a**, Upper left) to show the cells in OC. Bottom right, magnified view of (**a**, Upper right) to show the spatial painting of cell clusters from OC. Spots were colored by identity. (**b**) UMAP plot showing the cell clusters from OC colored by cell types, including interdental cell (IC), inner sulcus cell (ISC), inner phalangeal cell/inner border cell (IPhC/IBC), Hensen's cell (HC), outer sulcus cell (OSC), tympanic border cell (TBC), outer hair cell (OHC), inner hair cell (IHC) and Deiter cell_pillar cell (DC_PC). (**c**) Violin plots showing expression levels for a subset of genes used to classify cell types in (**b**). (**d-f**) Immunostaining of hair cells for the whole-mount cochlea at E17.5 (**d**), P8 (**e**) and adult (**f**). Myo7a is labeled in green; phalloidin, red; DAPI, blue. Scale bars equal to 200 μm. (**g**) Magnified view of (**f**) showing apical (upper), middle (middle), and basal (bottom) regions of adult cochlea, respectively.

Figure 6

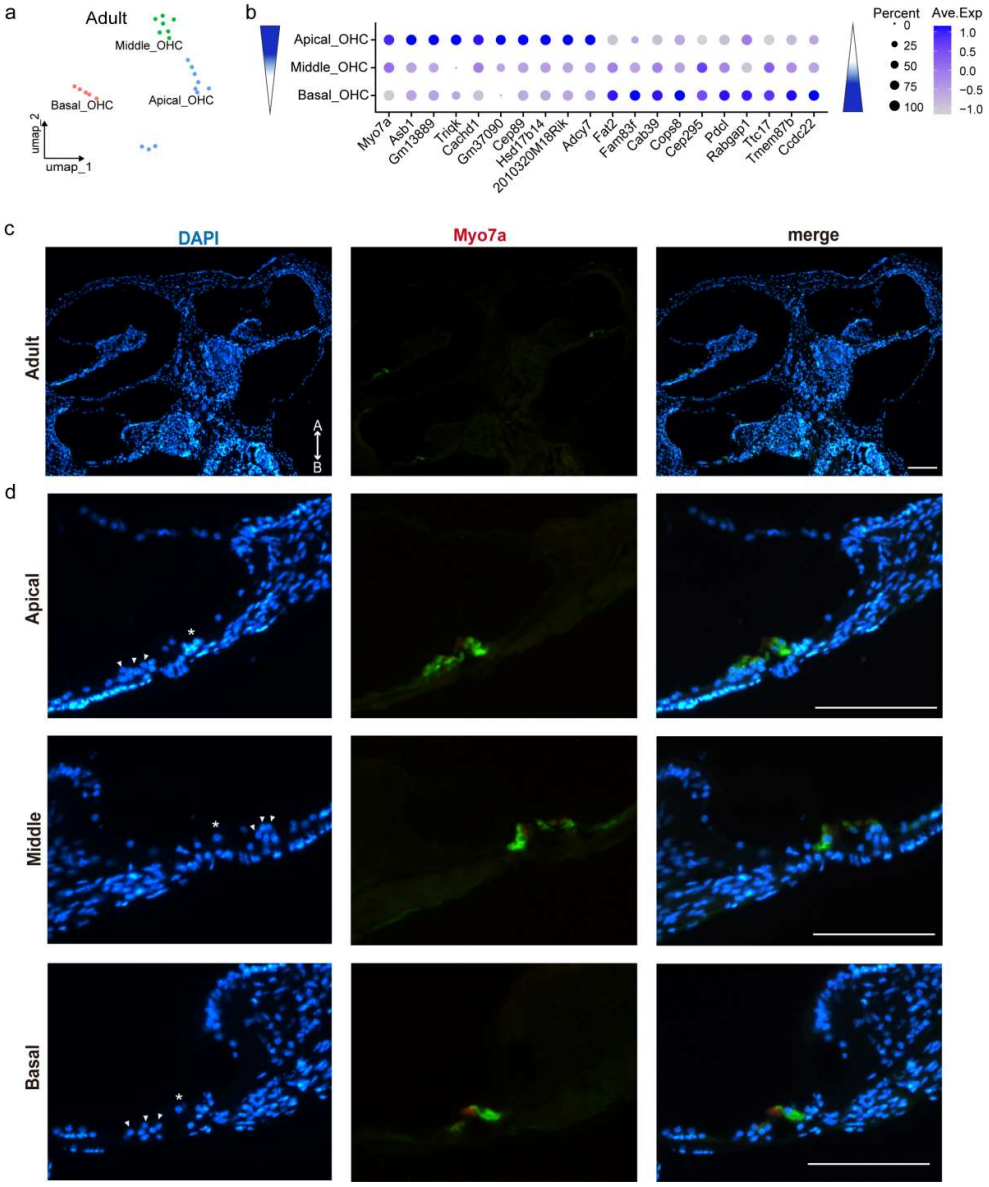

Fig. 6 Spatial differential analysis reveals gene expression gradients of OHCs from apex to base. (**a**) UMAP plot showing OHCs extracted from apical, middle and basal regions of P8 cochlea, colored by regions. (**b**) Bubble plot showing a number of gene expressions in OHCs with two gradient patterns (Apex-to-base decreasing or increasing expression). (**c**) Immunostaining of myo7a (green) on P8 cochlea section. DAPI is labeled in blue. Scale bar equals to 200 μm. (**d**) Magnified view of (**c**) to show staining

of hair cell in apex region (upper), middle (middle) and basal regions (bottom), respectively.

Figure 7

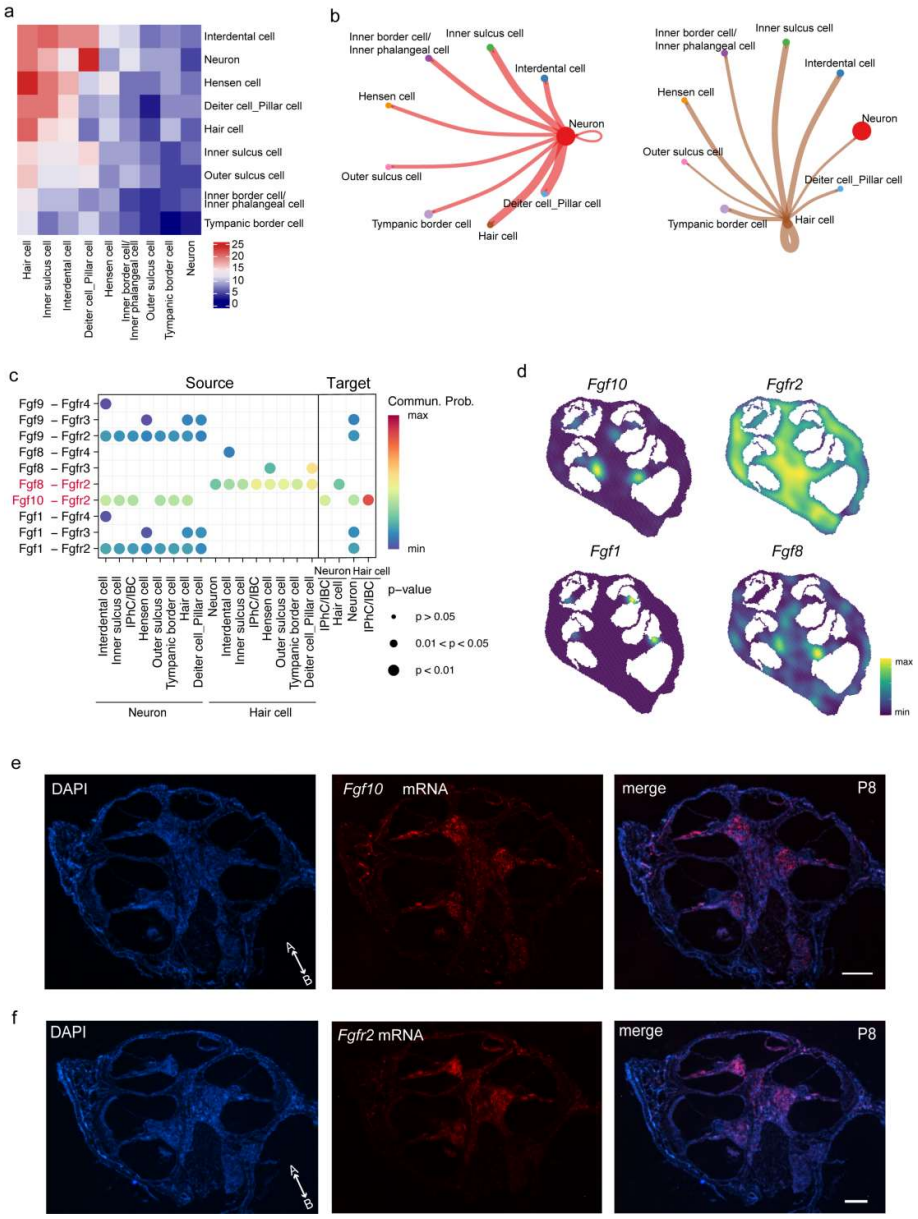

Fig. 7. Developmental dynamics of cell-cell communication network between cell clusters from the organ of Corti. (**a**) Heatmap showing the number of ligand-receptor pairs evaluated by cellchat for neuron cell and cell clusters from organ of Corti (OC) at P8. (**b**) Left, number of significant ligand-receptor pairs between cell clusters from OC at P8, with the neuron cell as a hub. Right, number of significant ligand-receptor pairs

between cell clusters from OC at P8, with hair cells as a hub. The edge width is proportional to the indicated number of ligand-receptor pairs. (**c**) Bubble plots showing ligand-receptor pairs of FGF signaling pathway between neuron cell and other cell clusters from OC. The size of dots represents the significance and the color represents the communication probability. (**d**) Spatial dense plots showing the expression level of *Fgf10*, *Fgfr2*, *Fgf1* and *Fgf8* at P8 cochlea section. (**e**,**f**) RNA *in situ* validating the expression of *Fgf10* mRNA (**e**) and *Fgfr2* mRNA (**f**) on P8 cochlea sections. Scale bar equals to 200 μm.

Figure 8

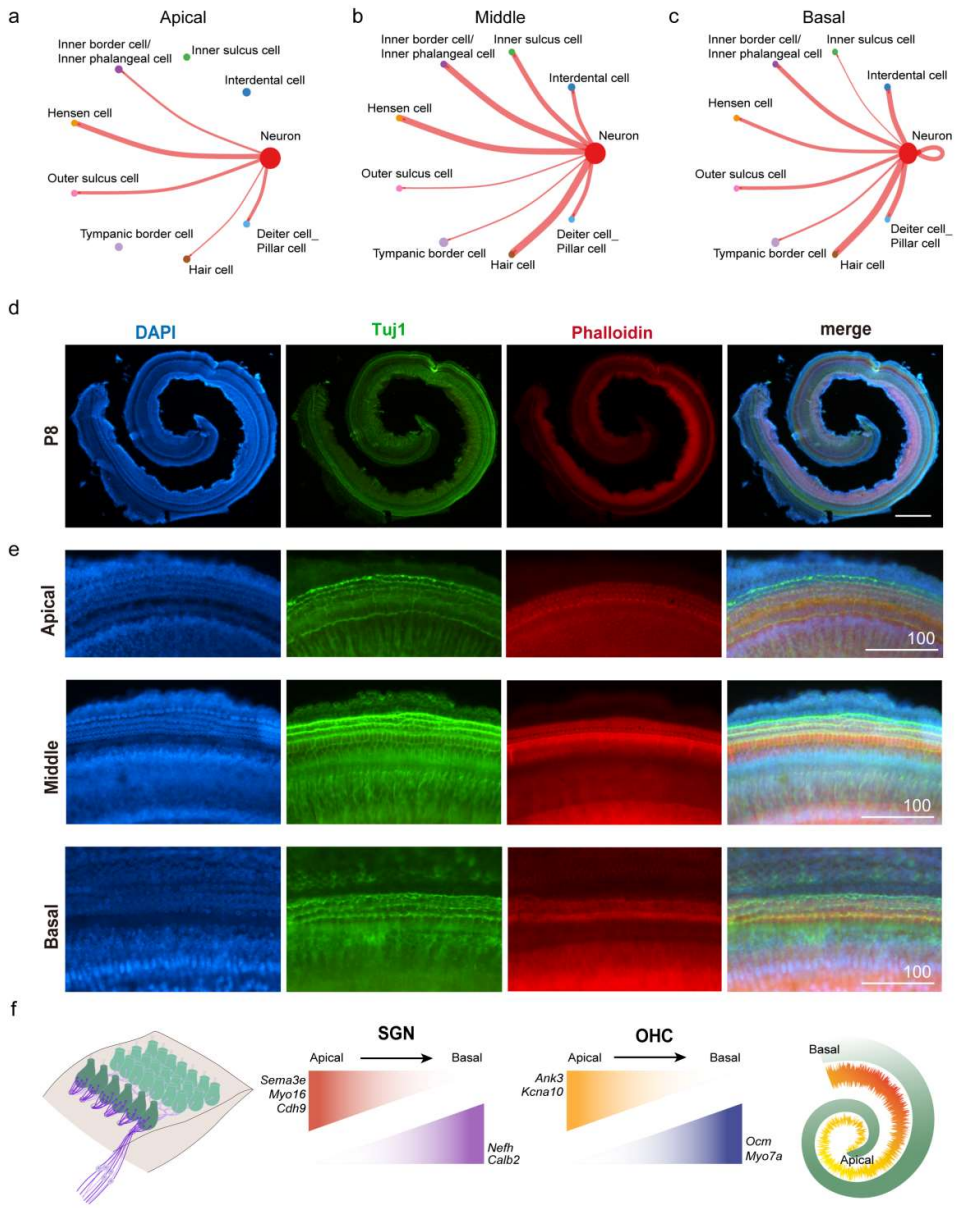

Fig. 8 Spatial cell-cell communication network from apex to base. (a-c) Number of significant ligand-receptor pairs between neuron cell and other cell clusters from OC located in the apical, middle and basal regions at P8, respectively. The edge width is proportional to the indicated number of ligand-receptor pairs. (**d**) The whole-mount immunostaining of Tuj1 (green) and phalloidin (red) on P8 cochlea. DAPI, blue. Scale

bar equals to 200 μm. (**e**) Magnified view of (**d**) to show neuronal connections and projections in apical (upper), middle (middle), and basal (bottom) regions, respectively. (**f**) Schematic representation illustrating the gradient patterning observed in hair cells and SGNs, highlighting a potential molecular mechanism underlying the tonotopic organization along the cochlear axis.

Figure S1

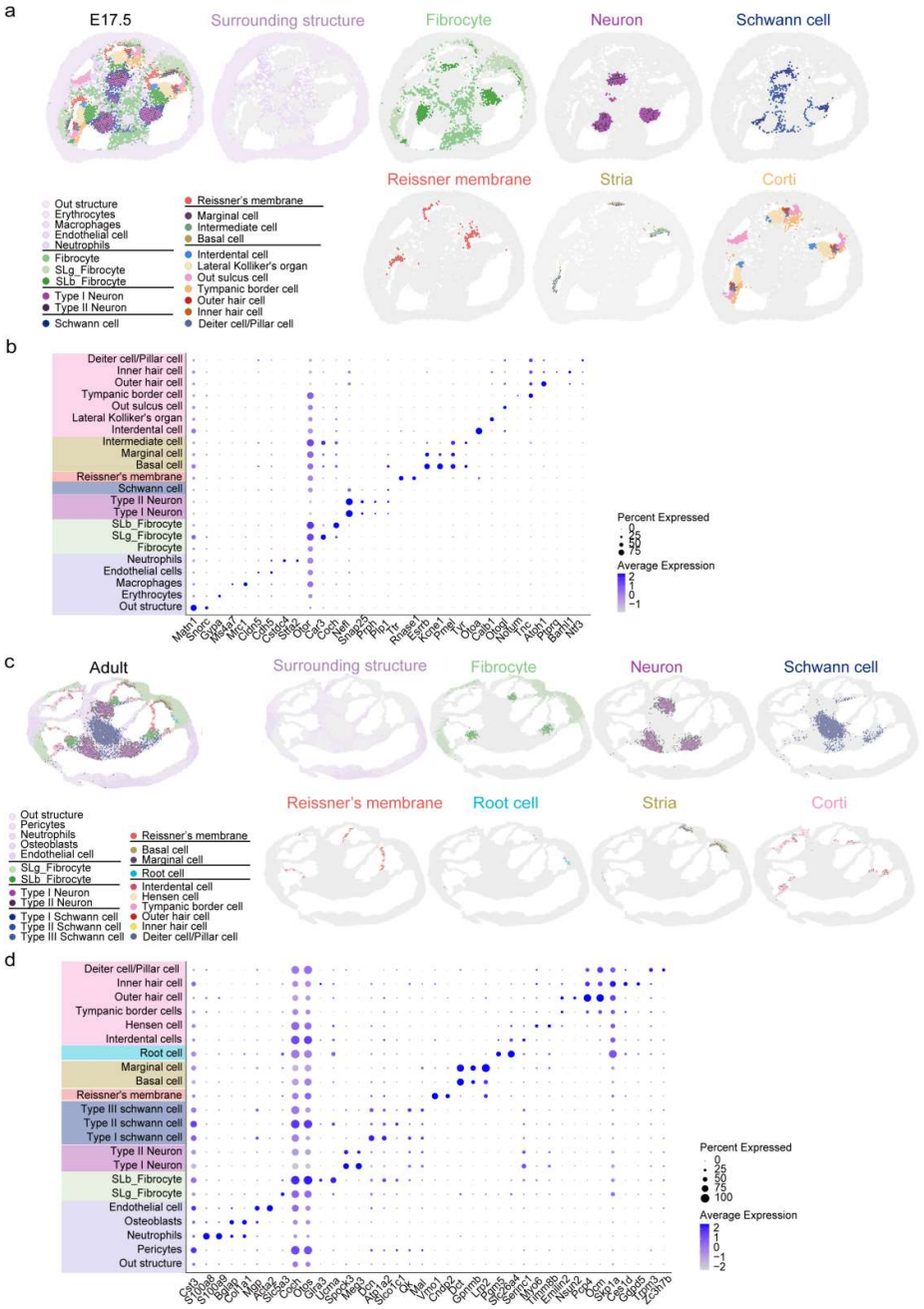

Fig. S1 Spatial single-cell atlas of developing and adult cochlea. (**a**) Spatial single cell types on the E17.5 cochlea cross-section. Eight major groups of cell types were shown, respectively. SLg: spiral ligament, SLb: spiral limbus. (**b**) Bubble plot analysis of the top differentially expressed genes for each cell types in the E17.5 cochlea. The

size of the dots represents the percentage of cells in the clusters expressing the gene and the color intensity represents the average expression levels of the gene in that cluster. (**c**) Spatial single cell types on the adult cochlea cross-section. Eight major groups of cell types were shown, respectively. (**d**) Bubble plot analysis of the top differentially expressed genes for each cell types on the adult cochlea. The size of the dots represents the percentage of cells in the clusters expressing the gene and the color intensity represents the average expression level of the gene in that cluster.

Figure S2

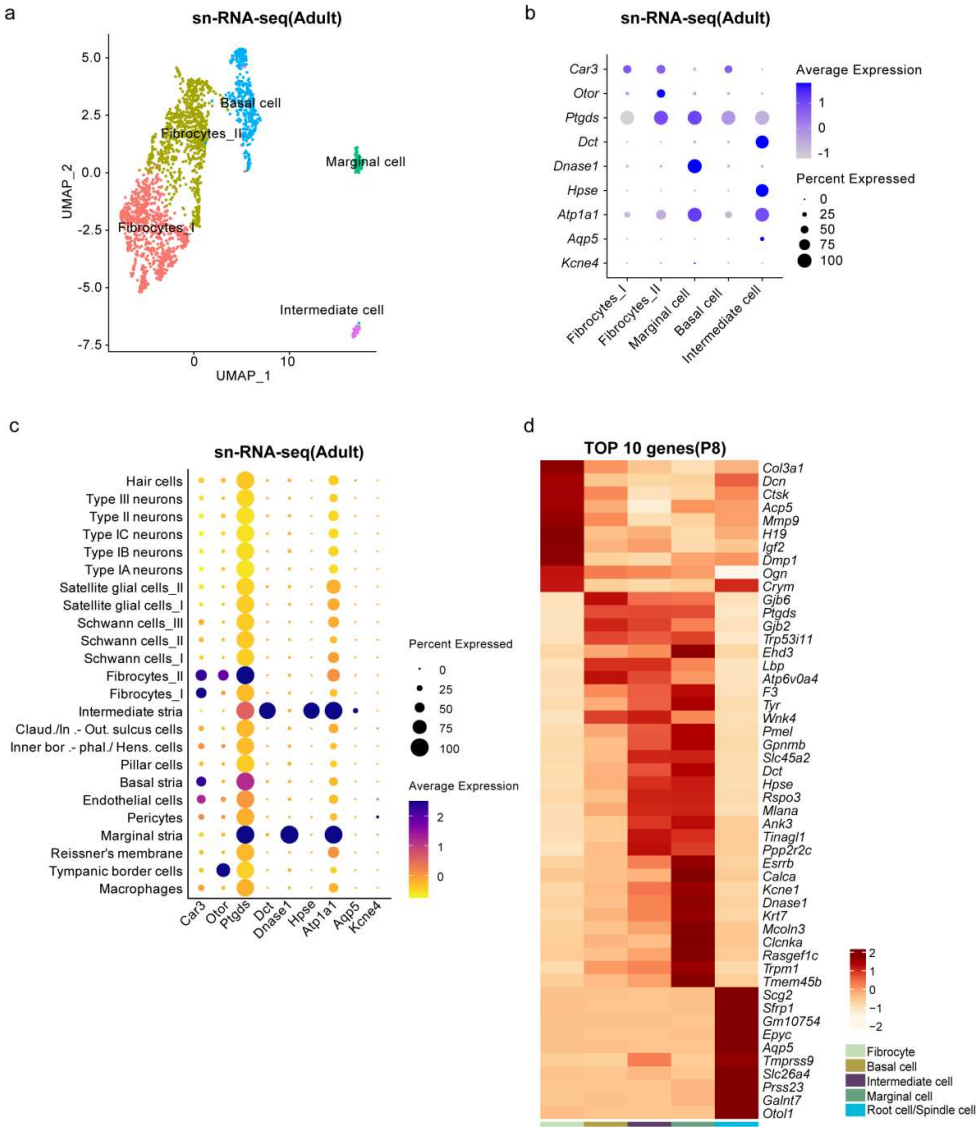

Fig. S2 Spatial analyses of lateral wall cell subtypes. (**a**) UMAP plot showing the lateral wall cells in the snRNAseq colored by cell types. (**b**, **c**) Bubble plot showing the markers from Fig. 2c in the snRNAseq dataset of cochlea. The size of the dots represents the percentage of cells in the clusters expressing the genes and the color intensity represents the average expression levels of the gene in that cluster. (**d**) Heatmap showing the expression level of the top 10 differential gene markers classifying the cell types from the lateral wall in the P8 spatial dataset.

Figure S3-1

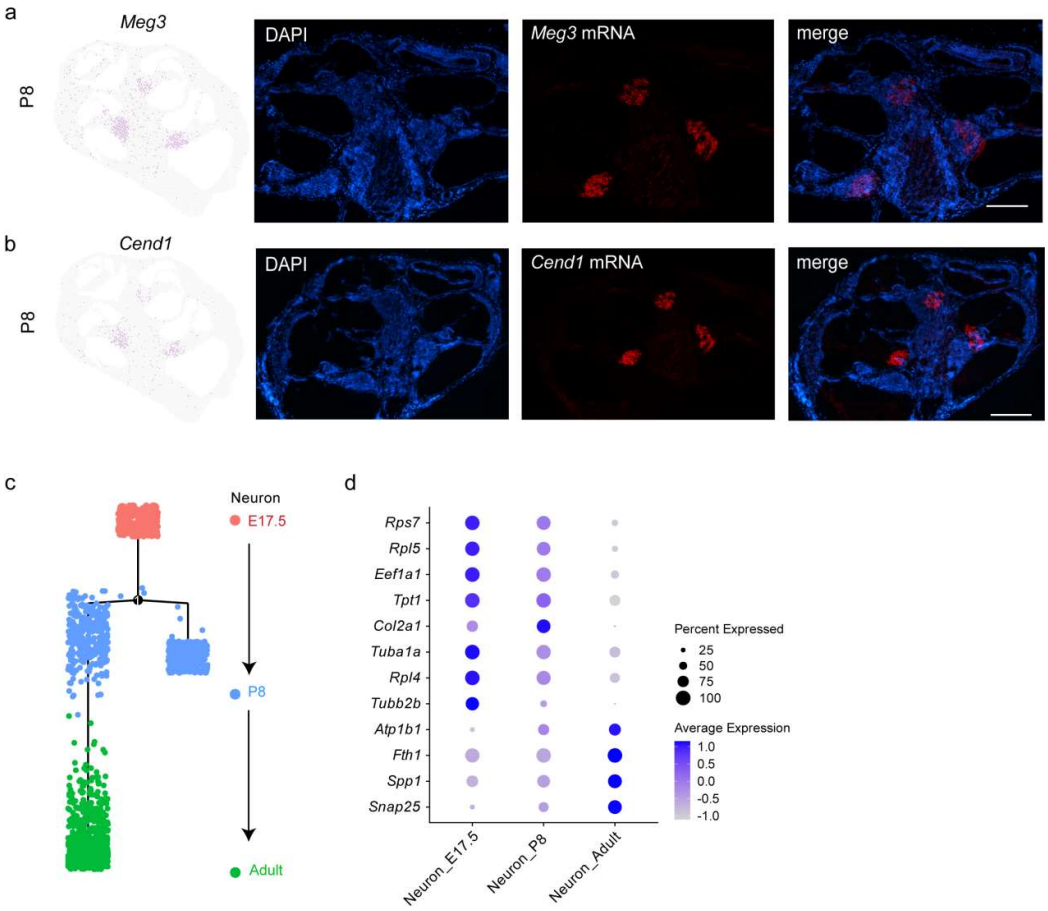

Fig. S3-1 Spatial dynamics of gene expression in spiral ganglion neurons. (**a, b**) Left, spatial expression of *Meg3* (**a**) and *Cend1* (**b**) on P8 cochlea spatial section chip. Right, RNA *in situ* detection of *Meg3* and *Cend1*mRNA on P8 cochlea section. Scale bar equals to 200 μm. (**c**) Dendrogram recapitulating the branched trajectory of the developing SGNs (E17.5, P8, and adult) based on the transcriptional similarity of pseudotime-ordered cells. (**d**) Bubble plot showing the differential expression of a set of genes in neuron cells at different development stages. The size of the dots represents the percentage of cells in the clusters expressing the genes and the color intensity represents the average expression levels of the gene in that cluster.

Figure S3-2

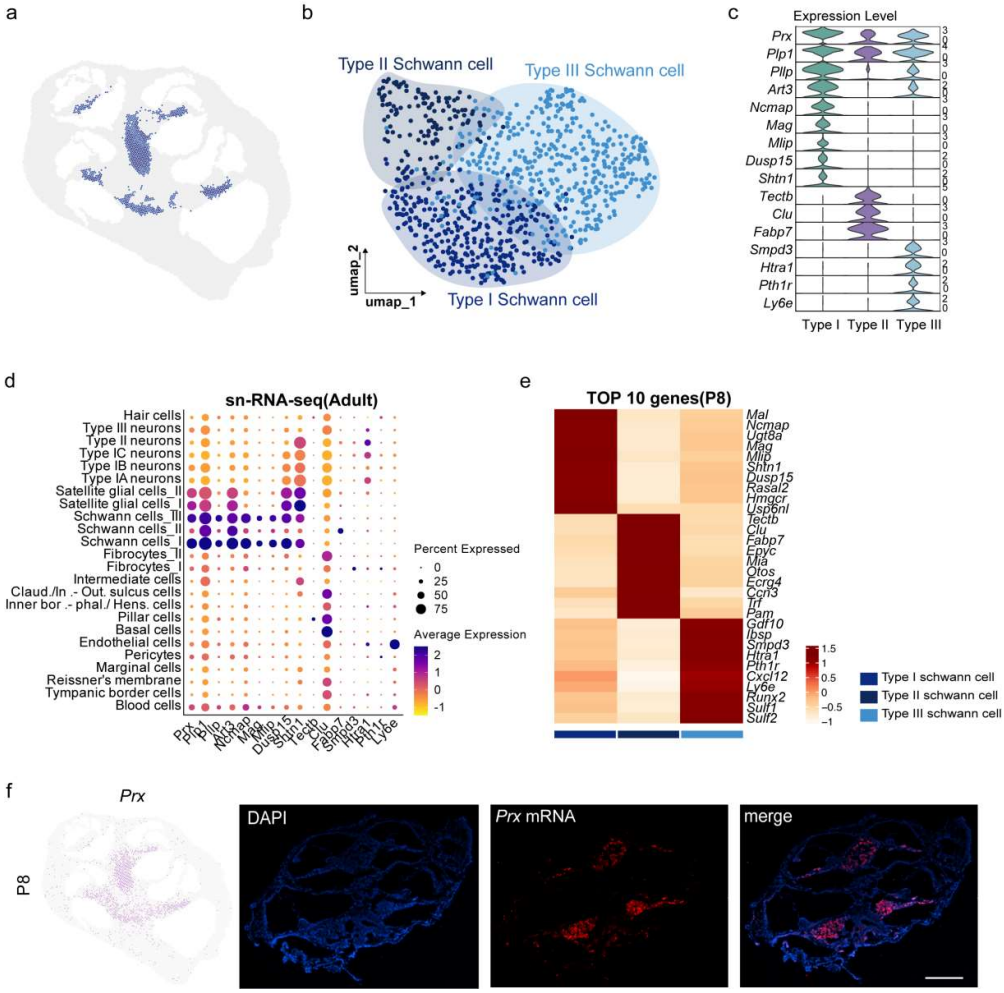

Fig. S3-2 Spatial expression pattern of Schwann cell subtypes. (**a**) Spatial distribution of Schwann cell at P8 cochlea. (**b**) UMAP plot showing the subtypes of Schwann cell at P8 cochlea colored by subtypes. (**c**) Violin plots showing the expression level of a set of genes classifying subgroups of the Schwann cell. (**d**) Bubble plot showing the expression level of genes from (**c**) in snRNA-seq dataset. The size of the dots represents the percentage of cells in the clusters expressing the genes and the color intensity represents the average expression levels of the gene in that cluster. (**e**) Heatmap showing the top 10 genes which were differentially expressed in the three

subclusters of Schwann cell in P8 spatial dataset. (**f**) Left, spatial expression of *Prx* at P8 cochlea, which specifically expressed in Schwann cell. Right, RNA *in situ* detection of *Prx* mRNA on P8 cochlea section. Scale bar equals to 200 μm.

Figure S4

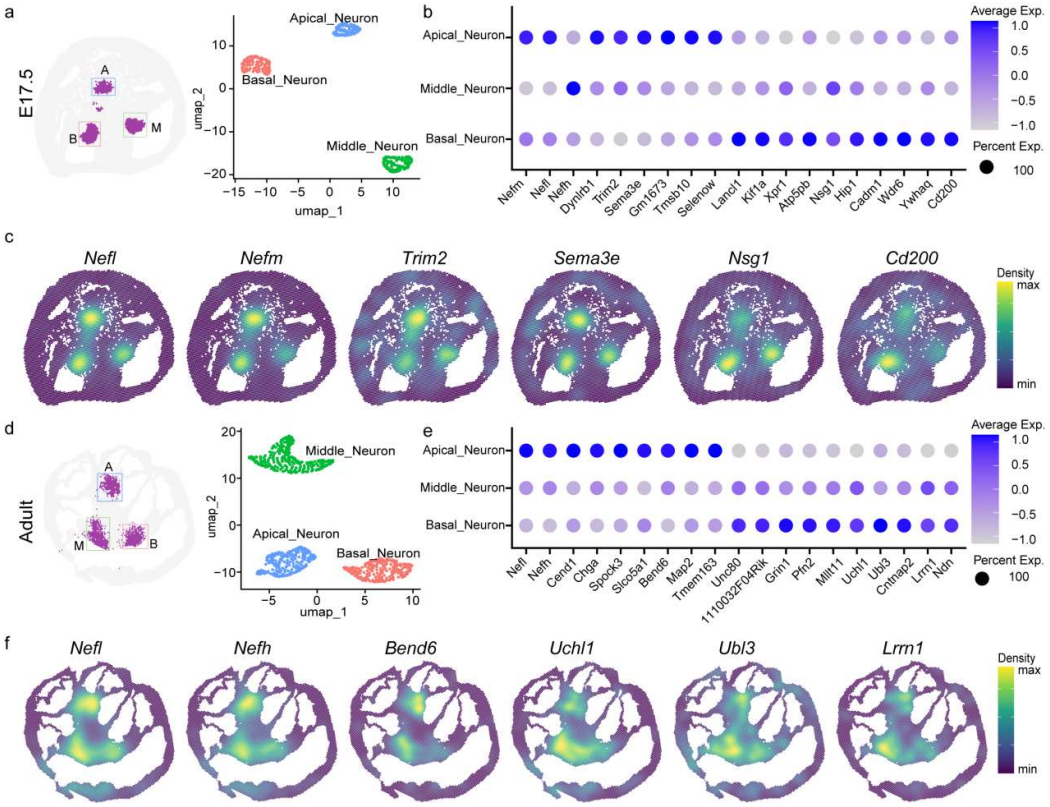

Fig. S4. Spatial differential analyses of neuronal expressing genes from apex to base. (**a**) Left, spatial distribution of neuron cells at E17.5 cochlea section chip, divided by rectangular boxes with different colors (three regions: A, apical; M, middle; B, basal). Right, UMAP plot showing the apical, middle and basal neurons extracted from E17.5 cochlea as shown on the left, as indicated by different colors. (**b**) Bubble plot showing the expression levels of the 19 genes in neuron cells from the three regions on E17.5 cochlea section, representing two gradient patterns (apex-to-base decreasing and increasing expression). The size of the dots represents the percentage of cells in the clusters expressing the gene and the color intensity represents the average expression levels of the gene in that cluster. (**c**) Density plots showing the spatial expression of *Nefl*, *Nefm*, *Trim2*, *Sema3e*, *Nsg1* and *Cd200*, on E17.5 cochlea section. (**d**) Left, spatial

distribution of neuron cells on adult cochlea section chip, divided by rectangular boxes with different colors. Right, UMAP plot showing the apical, middle and basal neurons extracted from adult cochlea spatial data as shown on the left. (**e**) Bubble plot showing the gradient expression of the 19 genes in neuron cells from the three regions on adult cochlea section, representing two gradient patterns (apex-to-base decreasing and increasing expression). The size of the dots represents the percentage of cells in the clusters expressing the genes and the color intensity represents the average expression of the gene in that cluster. (**f**) Density plots showing the spatial expression levels of *Nefl*, *Nefh*, *Bend6*, *Uchl1, Ubl3 and Lrrn1*, on adult cochlea sections.

Figure S5

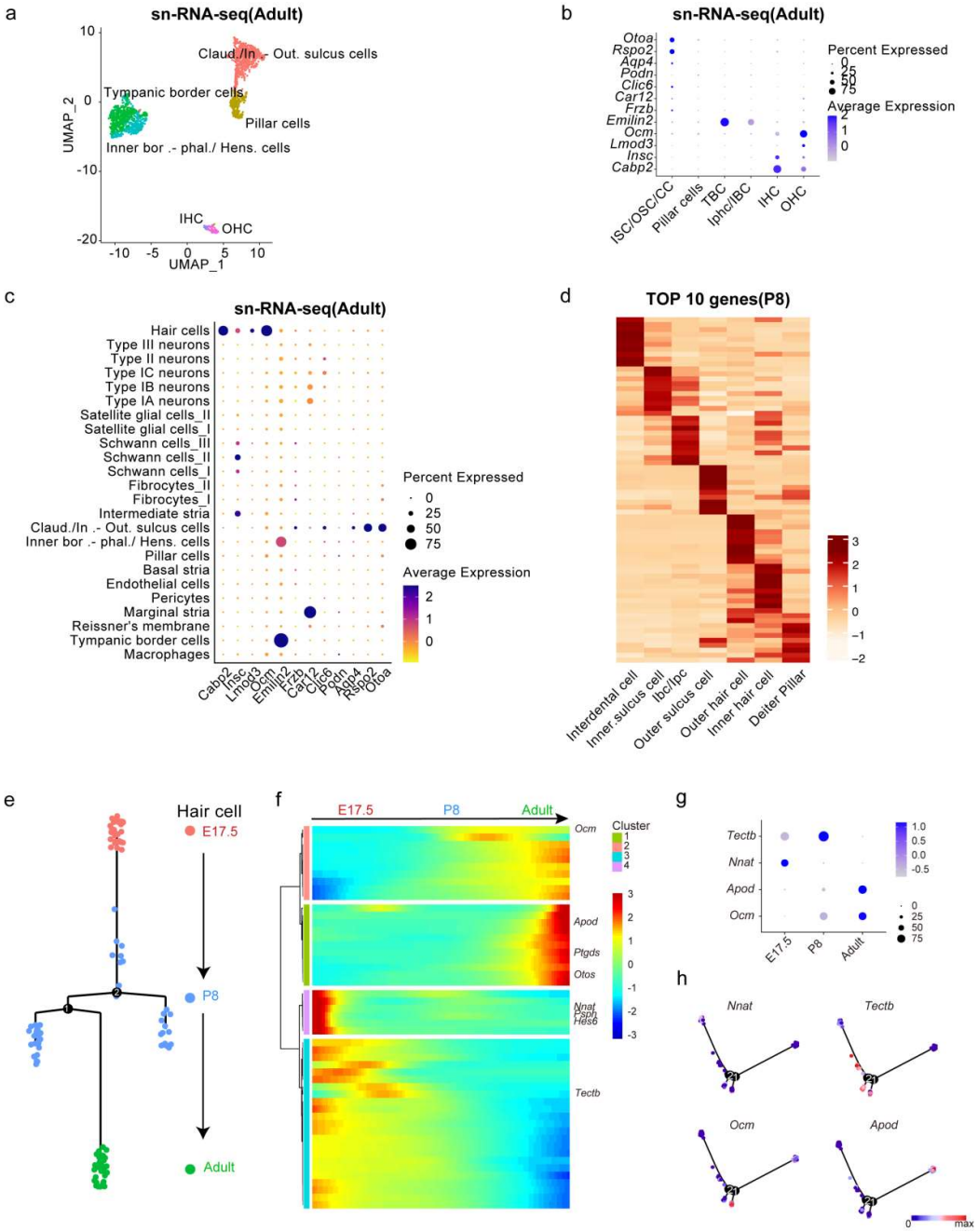

Fig. S5. Spatiotemporal analyses of cells from the organ of Corti. (**a**) UMAP plot for cells from OC group in our previous single nucleus RNA-seq dataset. (**b**, **c**) Bubble plot showing the expression levels of the marker genes from Fig. 5c in the snRNAseq dataset of cochlea. The size of the dots represents the percentage of cells in the clusters

expressing the genes and the color intensity represents the average expression level of the gene in that cluster. (**d**) Heatmap showing the expression levels of the top 10 markers classifying the cell types from the organ of Corti in the P8 dataset. (**e**) Dendrogram recapitulating the branched trajectory of the developing OHCs (E17.5, P8, and adult) based on the transcriptional similarity of pseudotime-ordered cells. (**f**) Heatmap showing overview analysis of the different trajectories, together with the top 50 up-regulated genes along the differentiation of each branch. (**g**) Bubble plot showing the differential expression of a set of genes in hair cells at different development stages. The size of the dots represents the percentage of cells in the clusters expressing the genes and the color intensity represents the average expression levels of the gene in that cluster. (**h**) Plots showing the expression of different genes in different hair cell trajectories.

Figure S6-1

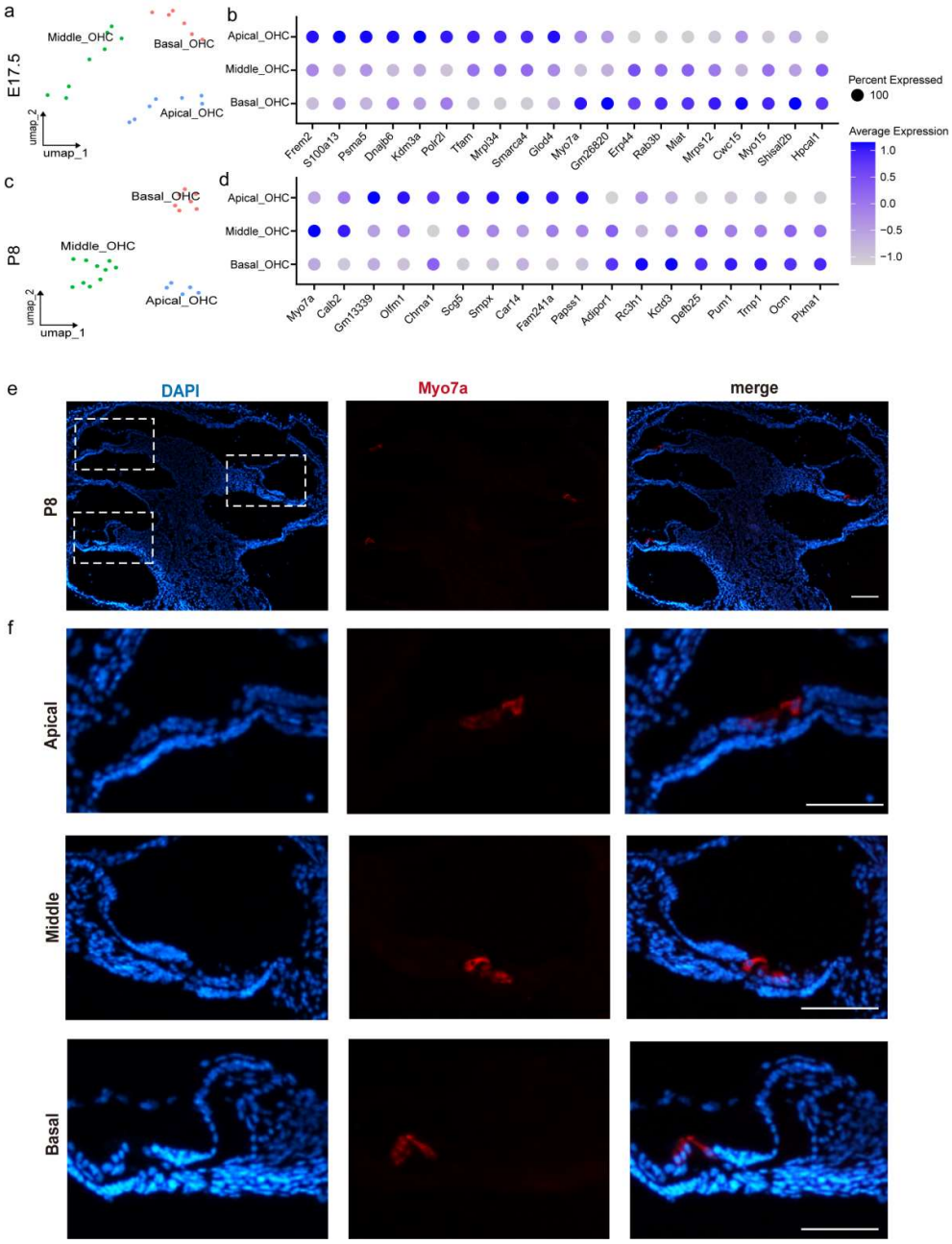

Fig. S6-1 Spatial differential analysis of OHC from apex to base. (**a**) UMAP plot showing OHCs extracted from apical, middle and basal regions of E17.5 cochlea. (**b**) Bubble plot showing the expression levels of a set of genes representing two gradient patterns (apex-to-base decreasing and increasing expression) in OHCs from E17.5

cochlea. The size of the dots represents the percentage of cells in the clusters expressing the genes and the color intensity represents the average expression levels of the gene in that cluster. (**c**) UMAP plot showing OHCs extracted from apical, middle and basal regions of P8 cochlea. (**d**) Bubble plot showing the expression levels of a set of genes representing two gradient patterns (Apex-to-base decreasing and increasing expression) in OHCs on P8 cochlea sections. (**e**) Immunostaining of Myo7a (red) on the P8 cross section. Dashed boxes indicated the apical, middle, and basal regions of the cochlea. DAPI is blue. Scale bars equal to 200 μm). (**f**) Magnified view of the dashed boxes in (**e**) to show the variant expression level of Myo7a in hair cells from apical (upper), middle (middle) and basal (bottom) regions, respectively.

Figure S6-2

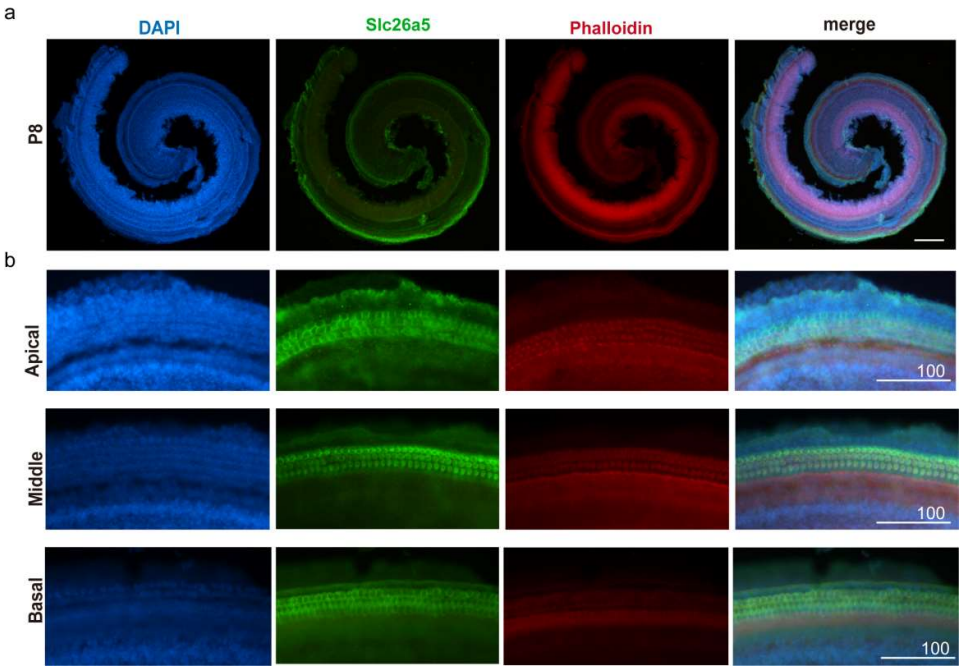

Fig. S6-2 Spatial differential analysis of OHCs from apex to base. (**a**) Immunostaining of Slc26a5 (green), and phalloidin (red) in the P8 whole amount cochlea. DAPI is blue. (**b**) Magnified view of (**a**) to show spatial differential expression of Slc26a5 in apex (upper), middle (middle), and basal (bottom) regions, respectively. Scale bar equals to 200 μm.

Figure S7-1

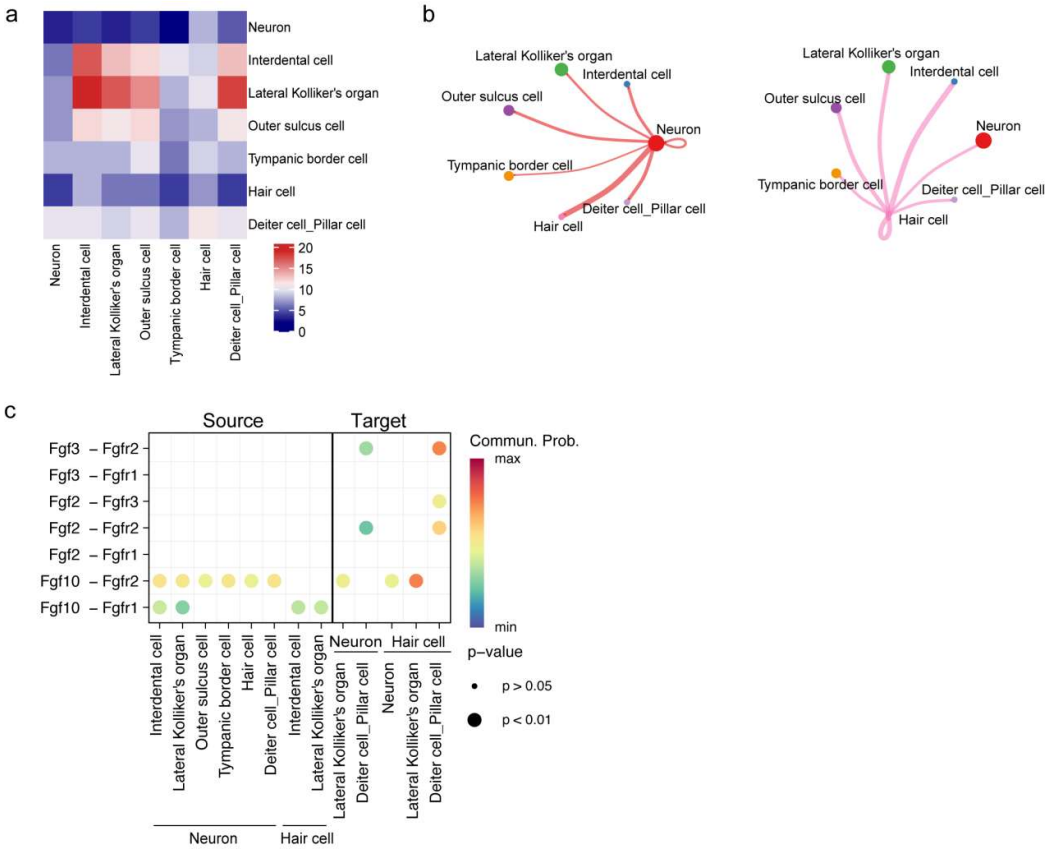

Fig. S7-1 Cell-cell communication network among neuron cell and cell clusters from Corti. (**a**) Heatmap showing the number of ligand-receptor pairs evaluated by cellchat for neuron cell and cell clusters from OC at E17.5 (**b**) Left, number of significant ligand-receptor pairs of neuron cells (hub) interacted with cell clusters from OC at E17.5. Right, number of significant ligand-receptor pairs between hair cells (hub) and neuron cells as well as other cell clusters from OC at E17.5. The edge width is proportional to the indicated number of ligand-receptor pairs. (**c**) Bubble plots showing ligand-receptor pairs of FGF signaling pathway between neuron cells and cell clusters from OC at E17.5. The size of dots represents the significance and the color represents the communication probability.

Figure S7-2

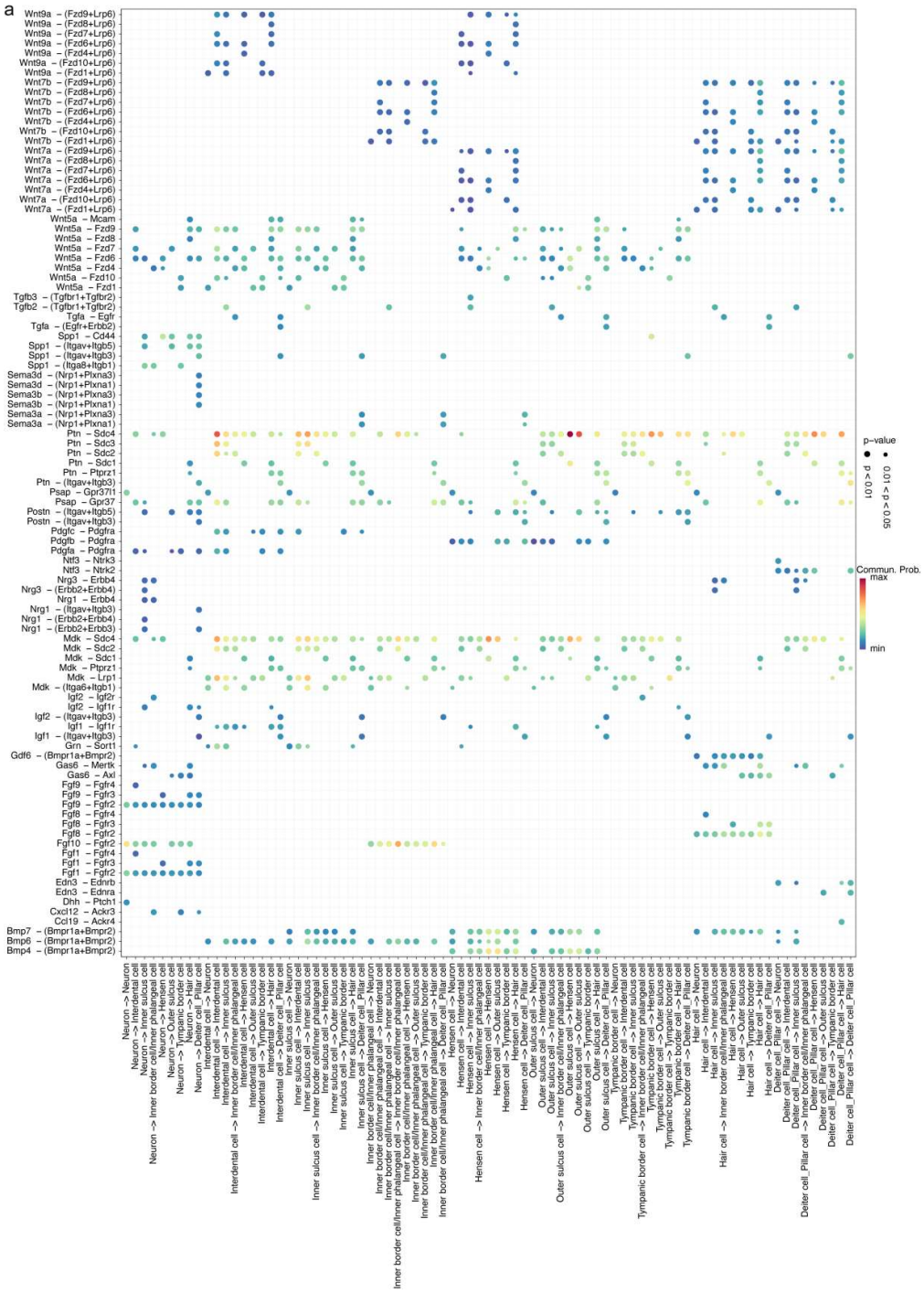

Fig. S7-2 Cell-cell communication network among neuron cell and cell clusters from the organ of Corti. Bubble plots showing ligand-receptor pairs between neuron

cells and other cell clusters from the organ of Corti for the P8 spatial data. The size of dots represents the significance and the color represents the communication probability.

Figure S8

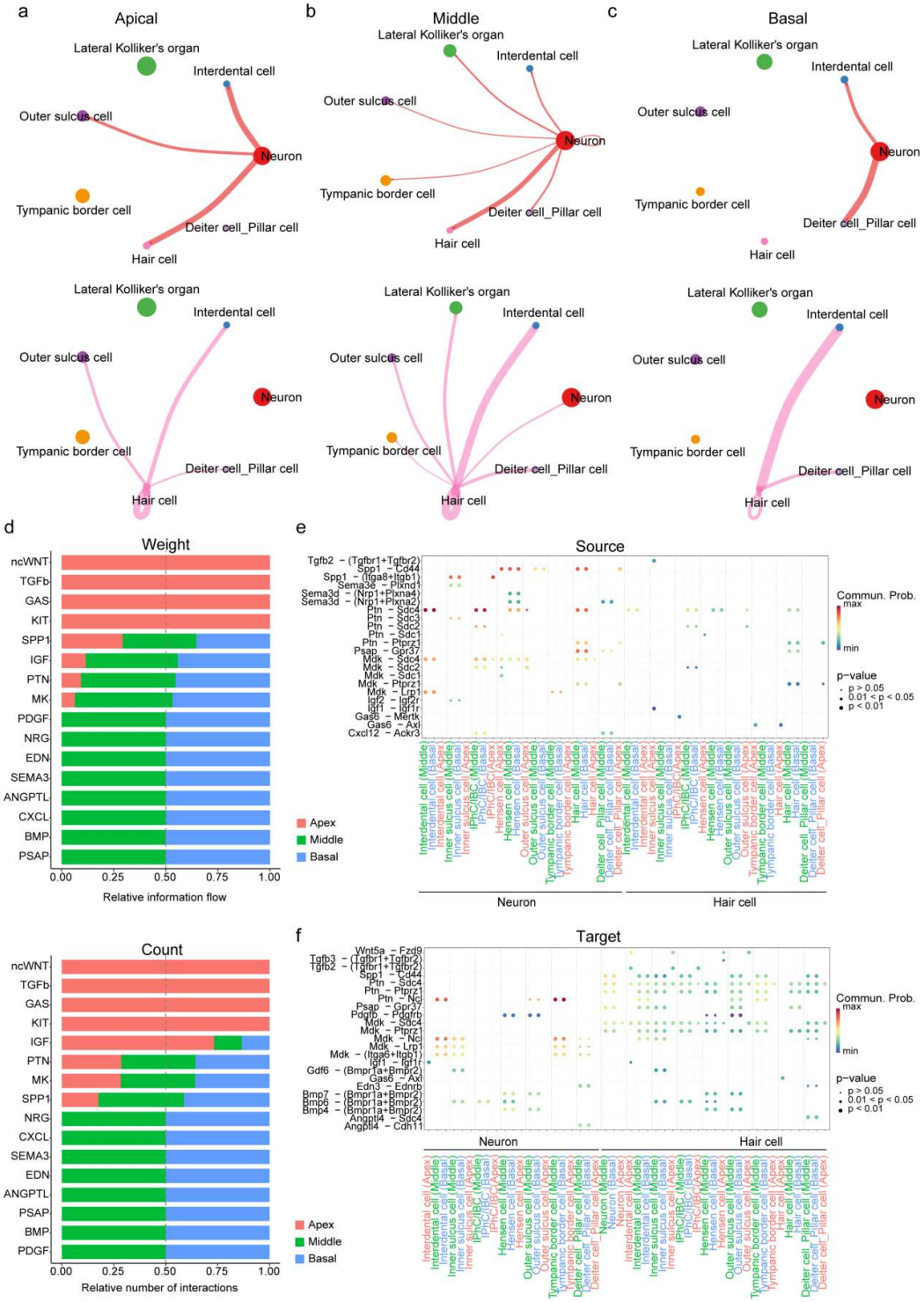

Fig. S8 Spatial cell-cell communication network among neuron cells and cell clusters from Corti. (a-c) Number of significant ligand-receptor pairs between neuron

cells and cell clusters from organ of Corti (OC) distributed in the apical (**a**), middle (**b**), and basal (**c**) regions at E17.5 stage, respectively. Up, the neurons are the hub; bottom, the hair cells are the hub. The edge width is proportional to the indicated number of ligand-receptor pairs. (**d**) Stack diagram comparing the weight (upper) and number (bottom) of interactions every signaling pathway predicted between neuron cells and cell clusters from OC distributed in the apical, middle and basal regions at E17.5 stage, respectively. (**e**) Bubble plots showing that neuron cells and hair cells are the source sending information to other cell clusters from OC in the different regions at E17.5 stage. The size of dots represents the significance and the color represents the communication probability. (**f**) Bubble plots showing the ligand-receptor pairs that neuron cells and hair cells are the targets to receive information from other cell clusters from OC in the different regions at E17.5 stage. The size of dots represents the significance and the color represents the communication probability.